REVIEW

Check for updates

Lanthanide-doped inorganic halide perovskites (CsPbX₃): novel properties and emerging applications

Santosh Kachhap,[a] Sachin Singh,[a] Akhilesh Kumar Singh*[b] and Sunil Kumar Singh (ID) *[a]

Inorganic halide perovskites (IHPs) have provoked intense research efforts because of their superior stability, excellent optoelectronic properties, cost-effectiveness, and striking optoelectronic applications. Recently, the doping of lanthanide ions in IHPs has opened new avenues, particularly for emerging applications like NIR and white light-emitting diodes, NIR emitters, NIR cameras, optical temperature sensing, optical data encoding, *etc.* Besides, lanthanide doping has also significantly improved the stability (thermal, photo, and phase), structure and optical properties of IHPs, which has resulted in improved device performance. However, a comprehensive review of this development for IHPs is rare. This review article is an attempt to fill this gap and is designed to provide important fundamental aspects as well as recent developments in the field. It comprises all the basics, synthesis strategies, crystal structure (including phase transition and phase stability), and optical properties (absorption, emission, lifetime, quantum yield, exciton binding energy, and anisotropy) for pristine IHPs with special reference to CsPbX₃ (X = Cl, Br and I). The effects of lanthanide doping on the above-listed properties for IHPs are explored, and the doping of non-lanthanide metal ions such as alkali metals, alkaline earth metals, transition metals, and post-transition metals in all-IHPs are also covered for comparison. Furthermore, the review specifically outlines a few novel applications, which are due to the inherent merits of lanthanide doping in CsPbX₃. Potential challenges and future perspectives are also discussed.

[a] Department of Physics, Indian Institute of Technology (Banaras Hindu University), Varanasi – 221005, India. E-mail: sunilks.app@iitbhu.ac.in
[b] Department of Physical Sciences, Banasthali Vidyapith, Banasthali, Rajasthan – 304022, India. E-mail: akhilesh_singh343@yahoo.com

Santosh Kachhap received the BSc degree in Physics in 2015 and the MSc degree in Physics (Electronics) in 2017 from Institute of Science, Banaras Hindu University, Varanasi. Uttar Pradesh, India. He was project fellow between January 2018– March 2019 at Indian Institute of Technology, Bhubaneswar, India. Currently he is working as a research scholar since 2019 in Luminescent Materials and Devices Development Laboratory,

Santosh Kachhap

Department of Physics, Indian Institute of Technology, Banaras Hindu University, Varanasi, India.

Sachin Singh received the BSc degree in Physics in 2016 from University of Delhi, Delhi, India, and the MSc degree in Physics in 2018 from University of Allahabad, Uttar Pradesh, India. Currently he is working as a research scholar since 2019 in Luminescent Materials and Devices Development Laboratory, Department of Physics, Indian Institute of Technology, Banaras Hindu University, Varanasi, India.

Sachin Singh

1. Introduction

Oxide perovskites are well known for their versatile applications in many fields, for example, in piezoelectricity, magnetism, superconductivity,[1-4] *etc.* In the last two decades halide perovskites have shown a paradigm shift in the application of perovskites.[5,6] Because of the direct bandgap, high absorption coefficient, high mobility, long carrier lifetime, cost-effectiveness, *etc.*, the all-inorganic cesium-lead halide perovskites ($CsPbX_3$, where X = Cl, Br, and I) have been considered as rising stars for photovoltaic applications.[7-11] They are also used in making colored and white LEDs,[12-15] fluorescence sensors,[16] oxygen detection sensors,[17] gas sensors,[18] humidity sensors,[19] field-effect transistors,[20,21] filter-free color image sensors,[22] display applications,[23] photodetectors,[24-26] spectro-chemical probes, explosive detectors,[27] laser fabrication,[28] X-ray detection,[29,30] *etc.* In this review, we mainly discuss the basics of halide perovskites, including the major advantages and challenges of halide perovskites. Detailed structural and optoelectronic properties of inorganic halide perovskites (IHPs) are also discussed. The study of the doping effect of lanthanide ions in the IHPs and their novel and emerging applications are the focus of this review. To study the various optoelectronic properties of all inorganic halide perovskites (IHPs), $CsPbX_3$ (X = Cl, Br, and I) has been chosen as a model system. Overall, the review article provides important fundamental aspects, as well as recent developments, in the field of IHPs.

Perovskites can be traced back to 1839 when a German scientist, Gustav Rose,[31] encountered a new calcium titanate-based mineral in the Ural Mountain, on a journey to Russia. The mineral was then named "perovskite" in honor of the renowned Russian mineralogist Lev von Perovski. The materials with a similar structure to $CaTiO_3$ are known as perovskites. The general formula of perovskites is ABX_3.[32] In the ABX_3 structure, A occupies the corner position, B is at the body-centered position,

Fig. 1 Structure of perovskite with formula ABX_3. Reprinted from ref. 32. Open access (2019).

and the face-centered positions are taken by the X atoms (see Fig. 1). The coordination number of B is 6, which is surrounded by the octahedral geometry formed by the X anions. The A atom has a coordination number 12 with cuboctahedral orientation. In general, the perovskites are characterized by the Goldschmidt tolerance factor, denoted as '*t*', as follows:

$$t = \frac{(r_A + r_X)}{\sqrt{2}(r_B + r_X)}$$

where r_A, r_B and, r_X are the ionic radii of atoms A, B, and X, respectively.[33] To form the perovskite structure, the *t* value should be between 0.8 and 1.0. The *t* value between 0.9 and 1.0 for the perovskite structure likely forms a cubic structure, with an ideal cubic structure at *t* = 1. Whereas, in the range 0.8–0.89, a perovskite with a distorted crystal structure (*i.e.*, orthorhombic or tetragonal or rhombohedra) is formed. If *t* is less than 0.8, the size of the B-site cation is too large to form a perovskite structure, and an alternative structure such as ilmenite-type (*e.g.*, $FeTiO_3$) is formed. Similarly, for *t* greater than 1, the B cation is too small to achieve the desired *t* value and in this case, the hexagonal structure is formed.

Dr Akhilesh Kumar Singh is working as an Assistant Professor in the Department of Physical Sciences, Banasthali Vidyapith, Rajasthan, India. He holds MSc in Physics (2004) from V.B.S. Purvanchal University, Jaunpur, India and MTech (2007) and PhD (2012) in Materials Science and Technology from Indian Institute of Technology (Banaras Hindu University) Varanasi, India. He worked as a Postdoctoral Fellow

Akhilesh Kumar Singh

in the UNAM, México, and University of Strathclyde, Glasgow. His research interests include hybrid halide perovskites, luminescent materials for energy harvesting, luminescent security inks, etc. He has published 43 peer-reviewed international journal papers and is a co-investigator of an Indian Patent.

Dr Sunil Kumar Singh is currently working as an Assistant Professor in the Department of Physics, Indian Institute of Technology (BHU), Varanasi, India (since 2018). His research is focused on spectroscopy of nanostructured materials and their technological applications in the area of photon upconversion, optical imaging, photovoltaics, optical and bio-sensors, etc. After completing PhD from Banaras Hindu University, India

Sunil Kumar Singh

(2011), he carried-out post-doctoral studies from Changwon National University, South Korea (2011–12). He also served as DST-INSPIRE Faculty at the Department of Physics, IIT (BHU) during 2013–2017. Dr Singh has contributed more than 50 articles having citations >2100 and h index-27.

Table 1 Classification of perovskite materials

	Oxide perovskite A = inorganic cation B = inorganic cation X = oxygen $SrTiO_3$,[40] $GdScO_3$,[41] $BaTiO_3$[42]	
		Organic–inorganic mixed halide perovskite $(MA/FAPbCl_{3-x-y}Br_xI_y)$ A = organic cation B = inorganic cation X = two or more halide anions $CH_3NH_3Pb(Br_xI_{1-x})_3$,[43] $CH_3NH_3PbCl_{0.5}Br_{2.5}$[44]
Perovskite ABX_3	Hybrid perovskite A = organic cation (MA^+, FA^+) B = inorganic cation X = halide anions	
	Halide perovskite A = organic/inorganic cation (Cs^+, MA^+, FA^+) B = inorganic cation (Pb^{2+}) X = halide anions (Cl^-, Br^-, I^-)	Organic–inorganic halide perovskite $(MA/FAPbX_3)$ A = organic cation B = inorganic cation X = one halide anion $HC(NH_2)_2PbI_3$,[45] $CH_3NH_3PbCl_3$[46] All-inorganic double perovskite $(Cs_2B^{1+}B^{3+}X_6)$ A = inorganic cation B = two inorganic cations X = one halide anion $Cs_2AgBiBr_6$,[47] $Cs_2InAgCl_6$[48]
	All-inorganic perovskite A = inorganic cation (Cs^+) B = inorganic cation X = halide anions	All-inorganic halide perovskite $(CsPbX_3)$ A = inorganic cation B = inorganic cation X = one halide anion $CsPbCl_3$,[49] $CsPbBr_3$,[50] $CsPbI_3$[51] All-inorganic mixed halide perovskite $(CsPbCl_{3-x-y}Br_xI_y)$ A = inorganic cation B = inorganic cations X = two or more halide anions $CsPbBr_1I_2$,[52] $CsPbCl_xBr_{3-x}$[53]

In recent years, a class of perovskites with the general formula ABX_3, where A and B are cations and X is the halide, has attracted a great deal of interest. In halide perovskites, A site atoms are either organic [MA^+: methylammonium $(CH_3NH_3^+)$, FA^+: formamidinium $(HC(NH_2)_2^+)$] or inorganic cations (Cs^+), whereas B is the metal cation (Pb^{2+}, Sn^{2+}, Ge^{2+}, etc.), and the X-site can have halides (Cl^-, Br^-, I^-).[34–36] When an organic cation (MA^+, FA^+, etc.) remains present at the A-site, it is called an organic–inorganic hybrid halide perovskite (e.g., $MAPbX_3$, $FAPbX_3$).[36–38] On the other hand, if an inorganic cation is present at the A-site, it is known as all-IHPs (for example, $CsPbX_3$).[39] The basic classes of perovskite structures, based on different types of atoms situated on A, B, and X sites, are listed in Table 1.

It is obvious from Table 1 that the halide perovskites are broadly classified into two categories, i.e., hybrid (organic–inorganic) halide perovskites and all-IHPs. The first hybrid halide perovskite reported for visible-light harvesting was methylammonium lead iodide ($CH_3NH_3PbI_3$) in 2009.[11] It shows high efficiency in photovoltaic applications, however, it suffers from poor phase stability (particularly in a humid atmosphere) and poor photo-stability.[54,55] It was found that the all-IHPs show better stability under different environments, e.g. humid atmospheres, light illumination, electric field, high temperature, and electron beam, etc.[56] Li et al.[10] carried out a comparative study of the stability of the hybrid halide perovskite and the all-IHPs in different atmospheres as listed in Table 2. The organic cations used in organic–inorganic halide perovskites, such as methylammonium and formamidinium, are among the major factors that result in phase instability.

Both the hybrid and the all-IHPs show bandgap tunability with changing the halide composition and through the variation of particle size, which eventually covers the entire visible spectral region (410–700 nm).[57–59] However, the all-IHPs show strong excitonic and spin–orbital coupling effects, resulting in spin-selective excitonic transitions, providing a new field for spintronics and quantum-optics applications.[59,60] Thus, researchers are intensively looking at all-inorganic metal halide perovskites, in which the organic cations of the hybrid perovskites are substituted with cesium ions, such as $CsPbX_3$ (X = Cl, Br, or I). The following sections in this review focus on the progress of $CsPbX_3$ perovskites and highlight the emerging applications.

This journal is © The Royal Society of Chemistry 2022

J. Mater. Chem. C, 2022, **10**, 3647–3676 | **3649**

Table 2 The stability comparison of hybrid and inorganic halide perovskites under different environmental conditions. Reproduced with permission from ref. 10. Copyright©2020, Elsevier

Environment	Hybrid halide perovskite	Inorganic halide perovskite
Humid	(1) Degrades into HI, PbI_2, and volatile organics	(1) Induces a phase transition and reversibly transforms into its initial phase by heating to 350 °C under humid conditions
Illumination	(1) Decomposes into PbI_2, metal lead, molecular iodine, and other volatile products	(1) Superior thermal and photochemical stability
	(2) Superoxide reacts with the protonated MA^+ and further decomposes its structure	(2) Acid protons are absent in Cs^+ ions and make their structure more stable
Electric field	(1) Migration barrier is lower under illumination	(1) Migration barrier is higher under illumination
	(2) Rapidly and irreversibly decomposes to PbI_2 under humid conditions	
High temperature	(1) The loss of organic components; perovskite degrades into PbI_2	(1) Phase transition in four different phases
Electron-beam	(1) Defect formation due to irradiation damage, and phase transformation induced by electron-beam heating	(1) Remain stable and does not degrade under the electron beam
	(2) Decomposes under the electron beam	(2) The intensity of the excitonic peak remains stable without the appearance of any high-energy peaks

2. All-inorganic halide perovskite CsPbX₃ (X = Cl, Br, or I)

2.1 Synthesis methods of CsPbX₃

There are various methods for synthesizing bulk and nano-structured all-IHPs. Nasstrom *et al.*[61] prepared $CsPb(Br_xI_{1-x})_3$ film, taking x between $x = 0$ and $x = 2/3$, using an inkjet printing technique, and $x = 0.85$ and $x = 1$ by spin coating. In another study, the efficient $CsPbBr_3$ perovskite film was developed for solar cell applications by using a single-crucible vacuum thermal evaporation method.[62] Recently, Borri *et al.*[63] reported the synthesis of $CsPbBr_3$ film of about 70 nm thickness by using RF-magnetron sputtering techniques on the glass substrate. In this method, the $CsPbBr_3$ powder, prepared by mechano-chemistry, is pressed for 24 hours by a pneumatic press (working pressure 11.5 MPa) and sputtering deposition was carried out at room temperature. The RF power of 20 W was maintained in an argon environment with a flow rate of 20 atm cm^3 min^{-1}. This is one of the powerful techniques for thin-film deposition, both for conductive and non-conductive materials, and may attract researchers in the future. Zhang *et al.*[64] synthesized $CsPbBr_{1.2}I_{1.8}$ nanocrystals (NCs) using the hot injection method. The colloidal solution of $CsPbBr_{1.2}I_{1.8}$ NCs was spin-coated at room temperature on a fused silica substrate. This formed a solid film and was used to study the light-induced phase segregations and optical studies. Liu *et al.*[65] used modified hot injection techniques to synthesize all-IHPs quantum dots (QDs). In this technique, the organolead compound trioc-tylphosphine–PbI_2 was swiftly injected into a 1-octadecene (ODE) solution, heated to 100–170 °C, which contained oleic acid (OA), oleylamine (OAm), and Cs-oleate.

All these methods have certain advantages and disadvantages. One common challenge observed in all the methods discussed above is poor long-term stability against moisture. However, the film deposited using the thermal evaporation method showed comparatively longer film stability.[66] The hot injection method, because of the requirements of high temperature and inert conditions, is neither cost-effective nor industrially viable.[15] However, it shows high thermal stability

and distinct optical features.[57] The single-crucible vacuum thermal evaporation techniques used by Li *et al.*[62] have advantages over multi-crucible vacuum thermal evaporation techniques. In multi-source (crucible) thermal techniques, the evaporation rate of the source material is highly dependent on parameters like the pressure of the vacuum chamber, the quality of evaporation materials, and the heating rate of the crucible. During the whole synthesis process, the adjustment of all these parameters for controlled evaporation is a difficult task so the single-crucible method is the best alternative to a multi-crucible method.

Thin-film deposition using the RF sputtering technique is suitable for both conductive and nonconductive materials.[63] It also provides uniform thin-film limited contamination and ease of doping. The major challenge of this technique is the controlled monitoring of parameters like pressure, deposition rate, and RF power to get a uniform thin film. In the modified hot injection method used by Liu *et al.*,[65] the particle size can be easily tuned by the injection temperature. In the modified hot-injection method, the organolead compound trioctylphos-phine-PbI_2 (TOP-PbI_2) is taken as the reacting precursor. Fig. 2 shows a comparative study of conventional hot injection and modified hot injection methods based on Stokes shifts and PLQYs. The all-IHPs prepared by conventional methods show noticeable Stokes shifts that also vary with the particle size. However, the modified hot injection method shows almost constant Stokes shifts for the different sizes of QDs indicated in Fig. 2(a). The absorption coefficient of TOP-$CsPbI_3$ QDs is higher than conventional OA/m-based $CsPbI_3$ QDs as shown in Fig. 2(b). The photoluminescence quantum yields (PLQYs) are stable for different sizes of QDs in the modified method.

The phosphine ligand-modified hot injection method was also reported by Li *et al.*[67] to improve the emission intensity and stability of $CsPbBr_3$ QDs under different atmospheres. The trioctylphosphine (TOP), tributylphosphine (TBP) and diphenyl-phosphine (DPP)-modified $CsPbBr_3$ QDs show high PL intensity and improved stability as compared to $CsPbBr_3$ QDs in ethanol, water and UV light irradiation. This may be attributed to the steric effect of the multi-branched phosphine ligand.
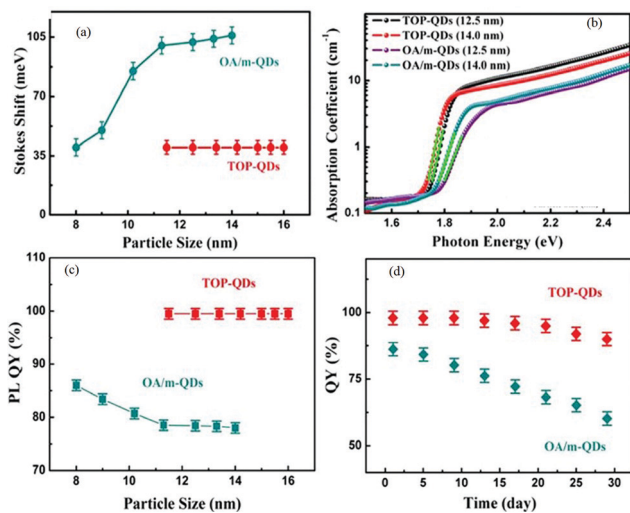
3650 | *J. Mater. Chem. C*, 2022, **10**, 3647–3676

This journal is © The Royal Society of Chemistry 2022

Fig. 2 (a) Stokes shift of the TOP-QDs and OA/m-CsPbI$_3$ QDs as a function of their particle sizes. (b) Optical absorption spectra of different sized TOP-QD and OA/m-CsPbI$_3$. (c) PLQYs of OA/m-QDs and TOP-QDs as a function of their particle sizes. (d) Change in the PLQY of the OA/m-QDs, TOP-QDs *versus* storage duration. QD solutions synthesized at 140 °C were stored in a sealed bottle under ambient conditions. Before the QY measurement, all QD samples were washed twice using MeOAc. Reproduced with permission from ref. 65. Copyright©2017, American Chemical Society.

2.2 Phase and phase transitions of CsPbX$_3$

Structure–property correlation makes it important to know about various phase transitions in halide perovskites. It affects the phase stability and the performance of devices like photovoltaic cells, light-emitting diodes, *etc.* The perovskite structure shows a stable cubic structure at high temperatures that switches to distorted metastable tetragonal and orthorhombic phases at low temperatures. The phase transition temperature depends on the perovskite composition and also to a lesser extent on sample preparation techniques. The formation enthalpy of different phases in the halide perovskite can be computed using the DFT method (even for the same composition) as follows:[68]

$$\Delta H_{ABX_3} = E_{ABX_3} - \mu_A - \mu_B - 3\mu_X \tag{1}$$

where E_{ABX_3} is the DFT calculated total energy, and μ_A, μ_B, and μ_X are the chemical potentials of the A, B, and X elements, respectively. In the perovskites, the lower symmetry structure has a more favorable formation enthalpy than the cubic structure. The orthorhombic structure *Pnma* phase has a lower formation energy and is the most commonly formed perovskite structure. The phase transitions in CsPbX$_3$ (X = Cl, Br, or I) are explained individually in Sections 2.2.1–2.2.3.

2.2.1 Phase transitions in CsPbCl$_3$. The phase transition in CsPbCl$_3$ has been studied by various groups using different methods such as neutron-scattering,[69] nuclear magnetic resonance,[70] differential thermal analysis (DTA),[71] temperature-dependent linear expansion and birefringence curves,[72] and differential scanning calorimetry (DSC),[73] *etc.* In CsPbCl$_3$, neutron-scattering and differential thermal analysis-based results suggest that the phase transition from the cubic to the

tetragonal phase occurs at 320 K, tetragonal to an orthorhombic phase at 315 K, and finally orthorhombic to the monoclinic phase at 310 K.[69,71] The DTA shows two anomalies, namely, an effectively larger one at 320 K and a relatively smaller one at 315 K, which are the consequences of the phase transition from the cubic to the tetragonal phase and the tetragonal to orthorhombic phase, respectively.[71] The temperature-dependent linear expansion and birefringence curves of CsPbCl$_3$ single-crystals also indicate sudden changes in the curves at about 310 K, 315 K, and 320 K.[72] These are clear evidence of phase transitions in the CsPbCl$_3$ single crystal. The phase transition in CsPbCl$_3$ has also been confirmed by the DSC technique.[73] A sharp peak was observed at 321 K and a small peak at about 316 K in a specific heat change *vs.* temperature graph, in good agreement with the phase transition temperature observed from other techniques.

2.2.2 Phase transitions in CsPbBr$_3$. For the study of phase transitions in CsPbBr$_3$, several methods, such as selected area electron diffraction (SAED),[74] neutron diffraction,[75] high-temperature X-ray diffraction,[76,77] and DSC,[76–78] have been used. Zhang et al.[74] studied phase transition in single-crystal CsPbBr$_3$ (synthesized using inverse temperature crystallization method) using the SAED patterns monitored through transmission electron microscopy (TEM) at various temperatures. The SAED patterns at different temperatures are shown in Fig. 3. The room temperature SAED pattern was characterized as the *Pbnm* space group of orthorhombic cells. On increasing the temperature, the phase transition from the orthorhombic to *P4/mbm* tetragonal structure was observed at 90 °C. Upon further increasing the temperature to 133 °C the transition from the tetragonal to the cubic structure was observed. However, CsPbBr$_3$ perovskite synthesized using the hot injection method showed an orthorhombic phase below 130 °C.[15] At temperatures above 130 °C, it showed a cubic phase that retained the same structure up to 200 °C. Rodova et al.[77] also studied the phase transition of CsPbBr$_3$ using high-temperature X-ray diffraction and DSC. At room temperature, it showed the orthorhombic structure (a = 8.207 Å, b = 8.255 Å, and c = 11.759 Å, *Pbnm* space group). The phase transitions from orthorhombic to tetragonal (a = 8.259 Å, b = 5.897 Å; *P4/mbm* space group) and tetragonal to cubic (a = 5.874 Å, *Pm̄3m* space group) were observed at 88 °C, and 130 °C, respectively. The neutron diffraction study carried out by Hirotsu et al.[75] also indicated the transition temperature from the cubic to tetragonal phase and tetragonal to orthorhombic phase at 130 K and 88 K, respectively. Thus, the synthesis technique and synthesis temperature both affect the phase transition in CsPbBr$_3$.

2.2.3 Phase transitions in CsPbI$_3$. Marronnier et al.[79] studied the phase transitions in CsPbI$_3$ halide perovskite and observed four different phases. Three of them have the perovskite structure α-*Pm̄3m* (cubic), β-*P4/mbm* (tetragonal), and γ-*Pbnm* (orthorhombic) and the fourth one δ-*Pnma* is a non-perovskite structure. The three perovskite phases of CsPbI$_3$, namely, the α, β, and γ-phases, are also called "black phases" and the non-perovskite δ-phase is called the "yellow phase".[80,81]

This journal is © The Royal Society of Chemistry 2022

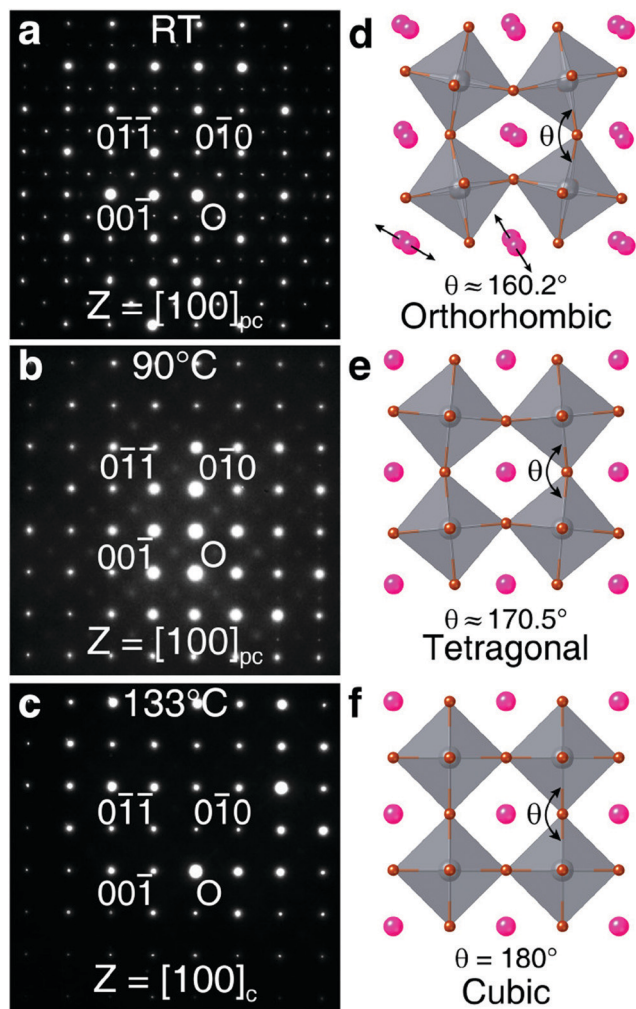*J. Mater. Chem. C*, 2022, **10**, 3647–3676 | **3651**

Fig. 3 The SAED patterns obtained for the CsPbBr$_3$ single-crystal at (a) room temperature, (b) 90 °C, and (c) 133 °C. (d–f) The orthorhombic, tetragonal, and cubic structures, respectively, for CsPbBr$_3$. Reproduced with permission from ref. 74. Copyright©2020, American Chemical Society.
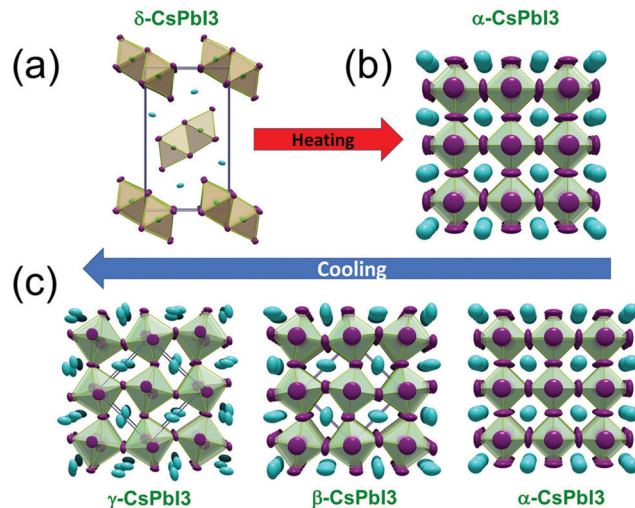

Fig. 4 The phase transitions in CsPbI$_3$: (a) the initial yellow non-perovskite δ-phase directly converts to (b) the black perovskite α-phase as the temperature exceeds the transition temperature on heating. (c) Upon cooling, the black perovskite α-phase undergoes various phase changes, namely, the tetragonal structure β-phase, orthorhombic structure γ-phase. These phases are metastable and finally transform into the thermodynamically stable δ-phase upon standing. Reproduced with permission from ref. 79. Copyright©2018, American Chemical Society.

Fig. 4 shows the crystal structures of all these phases. It was observed that on increasing the temperature, a direct phase transition from the non-perovskite δ-*Pnma* to the perovskite cubic *Pm$\bar{3}$m* phase occurred at 595 K.[79] This is a stable phase at high temperature. While cooling down, all the four crystal structures, cubic, tetragonal, orthorhombic, and non-perovskite, were observed. In the cooling process, the phase transition from the cubic perovskite structure α-*Pm$\bar{3}$m* phase to the tetragonal structure β-*P4/mbm* occurred at 539 K, the β-*P4/mbm* to ortho-rhombic structure γ-*Pbnm* was observed at 425 K and finally, the transition to the non-perovskite structure δ-*Pnma* phase occurred at room temperature. The bandgap of the non-perovskite yellow δ-*Pnma* phase was 3.01 eV and was stable at room temperature. The γ-phase orthorhombic structure was more stable under ambient conditions.[82,83]

A comparative study of the phase transition in CsPbX$_3$ indicates that the transition from the cubic structure to the tetragonal in CsPbCl$_3$, CsPbBr$_3$, and CsPbI$_3$ takes place at 320 K, 406 K, and 595 K, respectively.[68] The greater the size of the halide ion, the higher is the transition temperature. These transitions produce structural distortions in the crystal. The phase transition-induced structural distortions can be divided into three categories: (i) polar displacement of the A or B cations away from their high symmetry positions, (ii) rigid tilting of the corner-sharing BX$_6$ octahedra, and (iii) the collective Jahn–Teller distortion of the BX$_6$ octahedra.[68] The corner-sharing BX$_6$ octahedra tilting is associated with the size of the A-site cation and the ratio of the cavity volume to the A-site cation size. The smaller size A cation affects the Goldsmith's tolerance factor (t) and leads to a distortion in the network. Similarly, the larger the volume of the octahedral cavity to the size of the A-site cation ratio, the greater the tilting of the octahedra.

2.3 Stability of CsPbX$_3$

The stability of halides is one of the major concerns that can be changed by modifying its internal structure; *i.e.*, A and B-site cations, halide compositions, size reduction, and surface modification. As discussed, ions at A, B, and X-sites in the ABX$_3$ halide perovskite affects the value of the Goldsmith tolerance factor "t", and the octahedral factor ($\mu = r_B/r_X$), which determines the structure formed. The value of t between 0.8 to 0.9 forms the distorted perovskite tetragonal or orthorhombic structure, and between 0.9 to 1.0 most likely forms a cubic structure with the most stable α-phase cubic structure at $t = 1$.[21,84,85] According to the definition of t, the larger A-site cations favor higher t-values that make the halide perovskite structure more stable.[21,84] Cs$^+$ is almost the largest inorganic cation in the periodic table. Therefore, we cannot find a better

3652 | *J. Mater. Chem. C*, 2022, **10**, 3647–3676

This journal is © The Royal Society of Chemistry 2022

choice for its replacement in the periodic table for the synthesis of all-IHPs. Consequently, researchers have incorporated some organic cations into the $CsPbX_3$ but it produces a negative effect on the stability of the structure. The *t*-value greater than 1.0 implies that the size of the B atom is too small or the X atom is too large. Similarly, for *t*-value less than 0.8, the size of the B atom is too large or the X atom is too small to form a perovskite structure. These conditions lead to the formation of a non-perovskite structure.[86] In the ABX_3 perovskite structure, the B atom remains situated at the center of the octahedra formed by B and X atoms. The octahedral factor "μ" has an important role in octahedral stability. For the perovskite structure, the μ value should be $0.414 < \mu < 0.732$.[85] It plays a significant role in determining the size of the $[BX_6]^{4-}$ octahedral and the cuboctahedral voids. Thus, the factor *t* and the factor μ are interconnected for the structural determination in all-IHPs. Hence, the substitution of smaller sized cations at the B-site decreases the size of the octahedra and thus increases the *t* value, which results in an increased stability.[86] It has been reported that at room temperature, the stability of the halide perovskite increases from X = I to Br to Cl; *i.e.*, for smaller X-site ions.[87] All these halide perovskites are stable at the higher temperatures. The low stability of $CsPbI_3$ at low temperature is because of the tilting of the $[PbI_6]^{4-}$ octahedra, where the size of the cuboctahedral void available for the A-site atom is much larger than the Cs^+ atom.

The stability of all-IHPs is improved to some extent by the use of various organic surface-capping agents. Therefore, different organic compounds have been widely used to stabilize the perovskite structure.[88] In the synthesis of $CsPbX_3$ using the hot injection method, the Cs-oleate is injected *in situ* at elevated

temperature into octadecene (ODE) solution containing PbI_2, oleic acid (OA), and oleylamine (OAm). The particles are stabilized with both long-chain carboxylic and oleylammonium surface ligands.[65] In $CsPbI_3$ QDs, the ammonium ligands are easily lost because of the weak acid–base interactions arising between the I^- and oleylammonium during the essential purification procedures, resulting in a fast agglomeration and consequently a phase transformation from the α-cubic phase to a non-perovskite δ-phase.

The stability of the halide perovskite under a humid atmosphere and at elevated temperatures is of great concern. This can be increased by the surface modification by complex layers such as moisture-resistant layer(s), encapsulation, passivation, or by the use of additives.[89] Phenylethylammonium chlorine (PEACl), *p*-phenylenediammonium iodide (PPDI), and phenylethylammonium iodide (PEAI) have been widely used to address these concerns. They also improve the hydrophobic properties of all-IHPs and thereby stabilize the black phase perovskite structure. The hydrophobic alkyl chain or the conjugated heterocycle contained in the organic cations are believed to increase the humidity resistance.[90] The XRD patterns of $CsPbBrI_2$ and $CsPbBrI_2$-PEI thin films under different environmental conditions are shown in Fig. 5(a–c). The XRD pattern of the $CsPbBrI_2$-PEI thin film remains unaffected under $80 \pm 5\%$ relative humidity (RH) for 0.5 h and under heating up to 85 °C in an N_2 glove box for 72 h. Whereas, the $CsPbBrI_2$ treated under the same environmental conditions reflects significant changes in the intensity of XRD peaks, as well as the evolution of random peaks in the XRD pattern, which indicate poor stability under these environments. The significant improvements in the PL intensity for $CsPbBrI_2$-PEI was
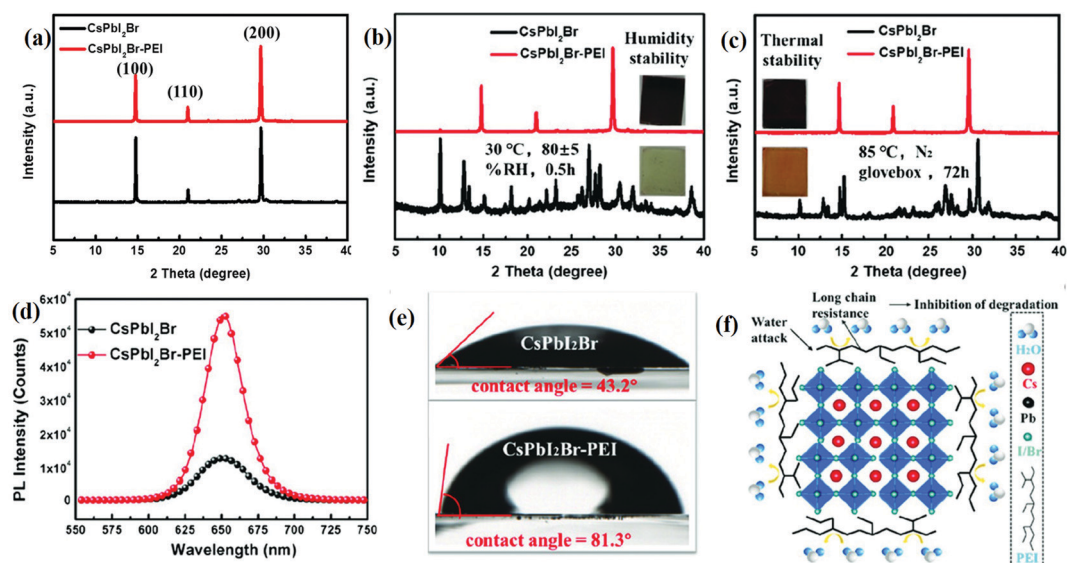

Fig. 5 The XRD spectra of the (a) $CsPbI_2Br$ and $CsPbI_2Br$-PEI thin-films. (b) $CsPbI_2Br$ and $CsPbI_2Br$-PEI films after being exposed to $80 \pm 5\%$ RH for 0.5 h (the inset shows images of samples after being exposed to $80 \pm 5\%$ RH for 0.5 h). (c) $CsPbI_2Br$ and $CsPbI_2Br$-PEI films heated at 85 °C in an N_2 glovebox for 72 h (the inset shows images of samples after heating at 85 °C in an N_2 glovebox for 72 h). (d) PL spectra of the $CsPbI_2Br$ and $CsPbI_2Br$-PEI thin films. (e) The water contact angles of $CsPbI_2Br$ film and $CsPbI_2Br$-PEI film. (f) A schematic diagram of the long-chain wrapping of $CsPbI_2Br$ grains. Reproduced with permission from ref. 90. Copyright©2020, Wiley Online Library.

This journal is © The Royal Society of Chemistry 2022

J. Mater. Chem. C, 2022, **10**, 3647–3676 | **3653**

also observed as indicated in Fig. 5(d). The CsPbBrI$_2$-PEI demonstrated hydrophobic behavior due to the long alkyl chain present at the grain boundaries, as shown in Fig. 5(f). The extent of hydrophobic character was measured by the contact angle and was 81.3° for CsPbBrI$_2$-PEI, and 43.2° for CsPbBrI$_2$. The XRD pattern of the CsPbBrI$_2$ film was completely transformed into the yellow phase under the relative humidity of 85% for 30 min but the CsPbBrI$_2$-PEI pattern remained unchanged, which confirmed the hydrophobicity characteristics as indicated in Fig. 5(e).[90] The CsPbBrI$_2$ film suffered phase transition from the α-phase (black color) to the δ-phase (reddish-brown color) due to thermal degradation in the N$_2$ environment. PEI effectively stabilized the CsPbBrI$_2$-PEI film during the annealing process and the α-phase was retained at this temperature as shown in Fig. 5(a–c).[90] The van der Waals forces among the PEI alkyl chains increased the crystal formation energy which resulted in enhanced phase stability. Polyethyleneimine (PEI) was used to reduce the defects in the all-IHPs, and it increased the phase as well as the structural stability of the CsPbBrI$_2$ perovskite against humidity and temperature.

Zhang et al.[91] used n-butylammonium iodide (BAI) in CsPbBr$_2$I to improve factors like the crystallization and morphology of the structure. The BAI incorporation decreases the trap state density and nonradiative recombination and thereby facilitates preparation at the reduced annealing temperature. An aromatic bi-functional ligand L-phenylalanine (L-PHE) in the in situ management of the present surface ligand environment stabilizes the phase of CsPbI$_3$ by coordinating with the cations and anions on the QD surface.[92] The L-PHE incorporated CsPbI$_3$ QDs also show improved PLQYs, and a longer lifetime, which provide longer diffusion length, high stability, and fewer trap states. This is advantageous in many applications like solar cells and LEDs, etc. Liu et al.[65] improved the stability of CsPbI$_3$ by using the organolead compound trioctylphosphine-PbI$_2$ (TOP-PbI$_2$) as a precursor. The room temperature quantum yield was up to 100%. The trapping defect centers, which contribute unwanted nonradiative recombination and result in luminescence quenching, are still a major problem in common quantum dots such as CdSe, and PbS, etc. Whereas, the TOP-PbI$_3$ precursor used for the synthesis of the CsPbI$_3$ QDs shows negligible electron or hole-trapping effects. This is evidenced by ultrafast kinetic analysis with time-resolved transient absorption spectroscopy.[65,93] In summary, the stability of the perovskite is improved to some extent by the use of various organic surface capping agents. At the same time, dimensionality also affects the stability of the structures.[13,87,94] The three black phases of CsPbI$_3$, α, β, and γ are metastable and likely to transform into the non-perovskite black δ phase. Steele et al.[94] reported that a thin film of the CsPbI$_3$ black phase is stable as compared to the bulk powder sample. Lower-dimensional perovskites are more stable than bulk 3D perovskite towards humidity.[95] This reflects that the stability can be improved by reducing the dimension of the structure.

2.4 Optical properties of CsPbX$_3$

2.4.1 UV-visible absorption and photoluminescence.
UV-visible absorption and PL measurement analyses are important

material characterization tools. One can observe the absorption features and gain information about transitions from various energy levels of atoms/molecules, and determine the optical bandgaps of the materials, etc., using absorption and PL measurements. The bandgap of halide perovskites can be tuned in the entire visible spectral region by changing the halide composition. The photographs of CsPbX$_3$ in hexane solution under room light (top) and UV lamp (bottom) illumination are shown in Fig. 6(a).[96] The CsPbX$_3$ (X = Cl, Br, I) showed absorptions in the wavelength region ranging from 390–680 nm.[57,96] The PL measurement showed that the emission maximum of CsPbCl$_3$ was ∼410 nm, which was further red-shifted after the partial/complete substitution of Cl$^-$ ions by Br$^-$ to I$^-$ ions.[57–59,96–100] The CsPbI$_3$ showed the lowest bandgap or highest cut-off absorption wavelength of ∼700 nm.[58,96] The absorption and PL spectra of all-IHPs with different halide compositions are shown in Fig. 6(b). These halide perovskites have narrow emission peaks with FWHM of 11 nm to 37 nm and, therefore, possess the high color purity required for various applications. Table 3 summarizes the emission peak position, FWHM, and PL quantum yields of CsPbX$_3$ halide perovskite as a function of halide compositions.

Apart from the halide concentration, the size of the NCs also affects the optical properties of all-IHPs.[57,101,102] With larger NCs, the emission peak and absorption band-edge shift towards longer wavelength. The size of the NCs also depends upon the cationic and anionic radii, larger ions increase the crystal size and vice versa for the same synthesis conditions. These effects were also observed in all-IHPs QDs. Fig. 7(a–c) show the variation in absorption and emission peaks of CsPbI$_3$ as a function of QDs size, and the corresponding morphologies are indicated in Fig. 7(d–f).[103] Similar variations in absorption and emission spectra were also observed in CsPbBr$_3$ QDs and are indicated in Fig. 7(g).[57]
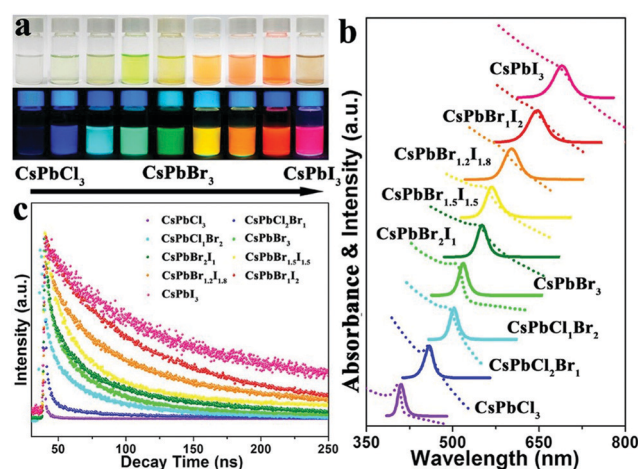
Fig. 6 Colloidal CsPbX$_3$ (X = Cl, Br, and I) NCs showing a change in the absorption and emission properties as a function of halide concentration. (a) Photographs of CsPbX$_3$ in hexane solution illuminated under room light (top), and UV lamp (bottom). (b) UV–visible absorption (dotted line), and PL spectra of CsPbX$_3$, and (c) PL lifetime of CsPbX$_3$ NCs. Reproduced with permission from ref. 96. Copyright©2017, American Chemical Society.

3654 | J. Mater. Chem. C, 2022, **10**, 3647–3676

This journal is © The Royal Society of Chemistry 2022

Table 3 PL properties of CsPbX$_3$ halide perovskites. Reproduced with permission from ref. 58. Copyright©2018, Nature

Sample	Emission peak (nm)	FWHM (nm)	PLQY (%)
CsPbCl$_3$	410	11.7	26.0 ± 0.3
CsPbCl$_2$Br	444	15.5	35.6 ± 0.4
CsPbCl$_{1.5}$Br$_{1.5}$	464	16.3	61.8 ± 0.4
CsPbCl$_1$Br$_2$	481	17.9	61.4 ± 0.8
CsPbBr$_3$	520	20.3	79.8 ± 0.9
CsPbBr$_2$I$_1$	587	28.2	71.2 ± 0.5
CsPbBr$_{1.5}$I$_{1.5}$	631	29.4	62.7 ± 0.2
CsPbBr$_1$I$_2$	660	29.9	58.5 ± 0.7
CsPbI$_3$	700	37.0	57.5 ± 0.4

The smaller the particle size, the higher the PLQYs, which is beneficial for light-emitting diodes.[65,104] Whereas, for the perovskite QDs with size less than the exciton Bohr diameter (D_B), the PLQYs decrease as observed by Kim *et al.*[105] PLQYs for 5 nm perovskite QDs was about 68%, and 62% for 3 nm. For the small perovskite QDs, the surface-to-volume ratio increased, which promoted the creation of surface traps for the exciton. This led to trap-assisted nonradiative recombination at the surface and resulted in a decrease in PLQYs. The variation in the bandgap with quantum dot size can be modeled using effective mass approximation (EMA), where the confinement energy is given by the following:

$$\Delta E = \frac{\hbar^2 \pi^2}{2m^* r^2} \qquad (2)$$

where m^* and r are the reduced mass of the exciton and the particle radius, respectively. The value of ΔE accounts for the blue-shift in the emission peak and absorption edge.[104] The bandgap of the CsPbBr$_3$ as a function of quantum dot size is shown in Fig. 7(h); the square box is the experimental data and the continuous line is the EMA model fitted curve.[57] A small Stokes shift, which is a measure of the energy difference between the peaks of exciton absorption and emission, was observed in all-IHPs. This indicates that a direct band-edge radiative recombination process is taking place in the resulting structure.

2.4.2 The optical bandgap and photoexcited exciton lifetime. In the CsPbX$_3$ perovskite, the valence band maximum (VBM) is formed by the antibonding interactions of Pb 6s and X np (n = 3: Cl, 4: Br, 5: I) orbitals dominated by X np orbitals.[106,107] The conduction band minimum (CBM) is formed by the antibonding interaction of the X np and Pb 6p orbitals, with the dominant contribution being from the Pb 6p orbital, whereas the A-site atoms have an almost negligible effect on the VBM and CBM. In CsPbX$_3$, for X = Cl to Br to I, the VBM shifts toward higher energies as the energy of the X np orbital increases, and at the same time, the CBM shifts towards the region of lower energies.[107] The orbital overlap between two atoms determining the bandgap of the configuration is inversely related to the sum of the ionic radii of the two atoms involved in bandgap formation. The sum of the ionic radii of Pb$^+$–Cl$^-$ is small as compared to the Pb$^+$–Br$^-$ and Pb$^+$–I$^-$,

Fig. 7 Optical properties and morphology of CsPbI$_3$ perovskite QDs. Absorption (black) and emission (red) spectra [(a–c)] of CsPbI$_3$ perovskite QDs with average sizes of 11.8 ± 1.6 nm, 10.8 ± 1.5 nm, and 6.5 ± 1.1 nm, respectively. (d–f) The corresponding TEM images of three QDs; scale bars in (d–f): 50 nm. Reproduced with permission from ref. 103. Copyright©2019, AIP Publishing. (g) Absorption and emission spectra of CsPbBr$_3$ plotted in the same image as a function of quantum dot sizes. (h) Variation of the bandgap of CsPbBr$_3$ as a function of quantum dot sizes, fitted with the EMA model. Reproduced with permission from ref. 57. Copyright©2015, American Chemical Society.

This journal is © The Royal Society of Chemistry 2022

J. Mater. Chem. C, 2022, **10**, 3647–3676 | **3655**

Table 4 Optical bandgap of various inorganic halide perovskites film

Perovskite structure	Optical bandgap (eV)	Synthesis techniques
$CsPbCl_3$	3.0	Chemical vapor deposition[110]
$CsPbBr_3$	2.33–2.34	Vacuum thermal evaporation[62]
$CsPbBr_2I$	2.05	Dual source thermal evaporation[111]
$CsPbI_{1.8}Br_{1.2}$	1.88	Spin coating[112]
$CsPbI_2Br$	1.9	One-step spray-coating[113]
$CsPbI_2Br$	1.86	Spin coating[112]
$CsPbI_{2.2}Br_{0.8}$	1.83	Spin coating[112]
$CsPbI_{2.4}Br_{0.6}$	1.80	Spin coating[112]
$CsPbI_{2.7}Br_{0.3}$	1.76	Spin coating[112]
$CsPbI_3$	1.7	Spin coating[114]

resulting in a high degree of orbital overlap and thus a higher bandgap in $Pb^+–Cl^-$. Table 4 summarizes the optical bandgap of some of the all-IHPs. The small variation in bandgap may be observed for the same composition when the synthesis method followed is different. However, if we change the A-site cation (keeping B and X site atom fixed) for comparison, it will affect the bandgap. The band of $FAPbI_3$ is 1.48 eV, which is less than the bandgap of $MAPbI_3$ (1.58 eV), whereas the bandgap of $CsPbI_3$ is 1.7–1.8 eV.[108] The bandgap of the FA-based hybrid perovskite $FAPbX_3$ is smaller than the MA-based $MAPbX_3$, and is smaller than $CsPbX_3$. In the MA-based hybrid perovskite, the bandgap changes from 2.28 eV ($MAPbBr_3$) to 1.58 eV ($MAPbI_3$) in $MAPbI_xBr_{1-x}$ on replacing Br with I;[109] however, the bandgap variation trend in $MAPbX_3$ is the same as $CsPbX_3$.

The variation in the photoluminescence quantum yields (PLQYs) in $CsPbX_3$ with halide composition has been studied by many groups. A literature survey indicated the clear trends of PLQYs from low to high with the partial or complete replacement of the Cl composition by Br, whereas, with the partial or complete replacement of Br by I, the PLQYs decreased. Based on the reported data, we predicted that the PLQY for the Cl-based all-inorganic halide perovskite ($CsPbCl_3$) was low and increased towards the Br-based all-IHPs maximum for $CsPbBr_3$; this again decreased towards I-based all-IHPs. As can be seen from Table 3, the PLQY value of the $CsPbCl_3$ is a minimum of about 26%.[58] It increased after the partial replacement of Cl^- ions by Br^- ions and attained the maximum value of about 80% for $CsPbBr_3$. Further, the substitution of I-ions at Br-sites resulted in a decrease in PLQYs as $CsPbI_3$ shows PLQYs of about 58%. However, the synthesis method and the type of precursor used for the synthesis of the particular $CsPbX_3$ perovskite affected the PLQYs as well as the stability.[115–118] Zhang et al.[115] used the phenyl-phosphonic dichloride ($PhPOCl_2$) as a "three precursor" source to synthesize the $CsPbCl_3$ NCs using the hot injection (usually two precursors are used) method. The $PhPOCl_2$ precursor-based $CsPbCl_3$ NCs showed 71% PLQYs with increased stability. Similarly, the use of surface capping agents and the dimensionality of the perovskite structure also affects the PLQYs and stability even for the same $CsPbX_3$ compositions.[116,119–122] Dutta et al.[116] reported the near-unity PLQYs in $CsPbX_3$ (X = Cl, Br, I) NCs. To achieve near-unity PLQYs, the oleylammonium halide was used as a precursor. The oleylammonium halide acts

as both a halide source and surface capping ligand and thus helps to increase the PLQYs of $CsPbX_3$ (X = Cl, Br, I) NCs by controlling the reaction temperature. The near-unity PLQYs was also achieved by doping metal ions into the all-IHPs discussed in the lanthanide and other metal ion-doped $CsPbX_3$ section.[123,124]

The photoexcited exciton lifetime is the time in which the number of electrons in the particular excited state is reduced to $1/e$ times the maximum population in that state. The radiative lifetime of the $CsPbCl_3$ is low and increases towards a high atomic number halide ion with maximum radiative lifetime for $CsPbI_3$.[57,96,125,126] The PL lifetime variation trends in all-IHPs with different halide compositions are shown in Fig. 6(c). The PL decay lifetime for $CsPbX_3$ in the band-edge exciton varies from 1.8–81.1 ns, measured by the pico-second pulsed laser of excitation wavelength 397 nm.[58] The PL decay lifetimes for $CsPbCl_{3-x-y}Br_xI_y$ are 1.8 ns, 3.5 ns, 8.9 ns, 8.2 ns, 21.1 ns, 41.1 ns, 66.2 ns, 75.0 ns, 81.1 ns for (x, y) = (0.0, 0.0), (1.0, 0.0), (1.5, 0.0), (2.0, 0.0), (3.0, 0.0), (2.0, 1.0), (1.5, 1.5), (1.0, 2.0), and (0.0, 3.0), respectively. It was observed that the all-IHPs with a large bandgap ($CsPbCl_3$) decays faster as compared to a low bandgap ($CsPbI_3$).[57] The radiative lifetime can be increased by reducing the thermal and concentration quenching effect. Thermal quenching is related to the temperature under analysis. Time-resolved PL study of $CsPbX_3$ QDs, prepared by using the organolead compound precursor trioctylphosphine-PbI_2 (TOP-PbI_2), showed that the photoexcited exciton lifetime was much longer, which is a clear indicator of the reduction of the quenching defects.[65]

2.4.3 Exciton binding energy and anisotropy. The coulombic attraction between electrons and holes is also attributed to exciton binding energy. The optoelectronic properties of semiconductors pretty much depend on their exciton binding energy.[127] In semiconductor nanostructures, the quantum confinement and the Coulomb interaction between electrons and holes are the two factors that affect the exciton binding energy. The quantum confinement depends on the nanostructure's size and shape. On the other hand, the Coulomb interaction is associated with the static dielectric constant of the material forming the nanostructure. Due to the confinement effect, the electrons and the holes localize, thereby increasing the exciton binding energy and oscillator strengths. The characteristic information about excitons can be obtained by applying external perturbation to the system, such as an electric or magnetic field. An applied magnetic field causes spin splitting of the spectroscopically observed energy levels and is directly proportional to the magnitude of the applied field. At the same time, it also increases the energy of the spin-split levels, called a diamagnetic shift. With an applied magnetic field, the quadratic energy shift in the exciton emission is observed. This gives information about the effects of quantum confinement and the Coulomb interactions in semiconductor nanostructures. In the presence of a magnetic field, the exciton energy is given as follows:[110]

$$E_\pm^n = E_0^n \pm \frac{1}{2} g_{\text{eff}} \mu_B B + \sigma_X^n B^2 \qquad (3)$$

3656 | J. Mater. Chem. C, 2022, **10**, 3647–3676

This journal is © The Royal Society of Chemistry 2022

where E_0^n is the nth exciton state unperturbed energy, g_{eff} is the effective exciton Lande factor, μ_B is the Bohr magneton, B is the applied magnetic field, and σ_X^n is the coefficient of the diamagnetic shift. The second term in the above equation represents Zeeman splitting, which increases the degeneracy of the exciton state. The third term represents the diamagnetic shift. The energy positions of the states $n = 1$ and $n = 2$ were fitted using the above equation, which gave $g_{eff} = 0.8$ and diamagnetic shift coefficient $\sigma_X^1 = 0.64 \pm 0.05$ μeV T^{-2} and $\sigma_X^2 = 2.0 \pm 0.2$ μeV T^{-2} for $CsPbCl_3$. The diamagnetic shift coefficient for $CsPbCl_3$ (high bandgap perovskite) is lower than $CsPbBr_3$ and $CsPbI_3$ (low bandgap perovskites).[83] The low value of the diamagnetic shift coefficient for $CsPbCl_3$ is due to the higher binding energy and lower Bohr radius.[110]

Another important aspect of $CsPbX_3$ is their anisotropic behavior that indicates a change in the different properties in different crystallographic directions. Zhao et al.[128] studied the Young's moduli of $CsPbI_3$ and $CsPbBr_3$ along different directions, which were found to be the same. On the other hand, $CsPbBrI_2$ and $CsPbBr_2I$ showed the isotropic nature of Young's moduli along the [001] and [010] directions, and along the [100] and [010] directions, respectively (see Fig. 8). In $CsPbBr_2I$ and $CsPbBrI_2$, the transport properties (electron and hole mobilities) are superior along [001] in both structures. In this direction, fewer carriers can be captured by the traps during transport. The superior properties of the crystal with [001] orientation may be more suitable for the applications of transistors, light-emitting diodes, photodetectors, solar cells, etc. Optical properties such as the extinction coefficient and refractive index of $CsPbBr_2I$ and $CsPbBrI_2$ also show anisotropic behavior. The extinction coefficients of $CsPbBr_2I$ and $CsPbBrI_2$ along the [001] direction are greater than that along the [100] direction. Therefore, photon absorption along the [001] direction is greater, resulting in the larger current density and better

spectral responsibility that are required in optoelectronic applications.

The anisotropy-dependent photo-response properties in $CsPbBr_3$ single-crystal thin-film have been studied by Wang et al.[89] The $CsPbBr_3$ film showed anisotropic behavior towards absorption and emission spectra, also verified by using first-principles studies. The absorption and emission intensity of $CsPbBr_3$ film on ZnSe were recorded using circularly polarized light in different polarization directions. The absorption and emission reached their maximum values for the polarization angle 0° while the minimum was observed for 90°. On moving the polarization angle from 0–180°, these again reached a maximum value at 180°. The polarization-dependent photosensitivity of the sample reported was 200 A W^{-1}, showing a fast photo-response time of 20 ms, and the current ratio for the on/off mode was about 10^4. The anisotropy-dependent absorption, emission and photoresponsivity of the film are indicated in Fig. 9(a), (b) and (c), respectively.

The anisotropy-dependent optical parameter variations were also observed in the nanowires (NWs).[130] The PL of $CsPbBr_3$ NWs was studied by applying a polarized excitation field E_0 perpendicular to the long axis of $CsPbBr_3$ NWs. The PL spectra of 15 nm thick and 250 nm thick NWs excited at 405 nm for polarization angles of 0° and 90° are shown in Fig. 10(a). The polar plots of the polarization-dependent PL intensity of 15 nm thick and 250 nm thick NWs excited at 405 nm are shown in Fig. 10(b) and (c), respectively. Fig. 10(d and e) are the respective optical PL images of two NWs of thickness 15 nm (scale bar 250 nm), and 250 nm at different polarization directions. It was observed that the PL intensity in the parallel polarization is five times higher than the perpendicular polarization for 15 nm thick NWs, which confirmed the anisotropy effect. The thickness-dependence study of NWs showed that higher anisotropy was attained for 15 nm thick NWs as compared to 250 nm thick NWs.

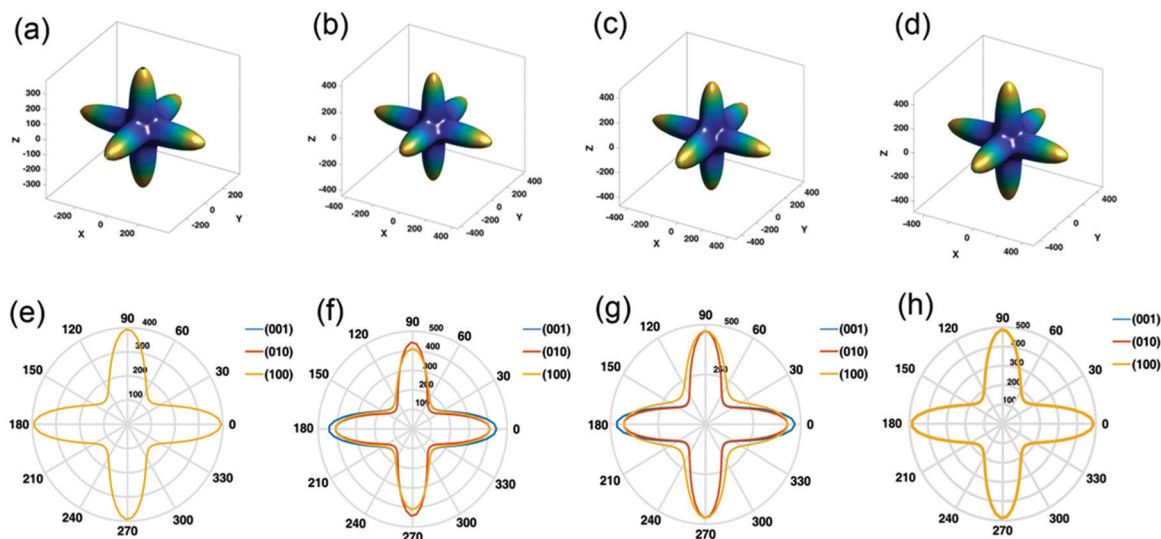**Fig. 8** 3D Young's modulus: (a) $CsPbI_3$, (b) $CsPbI_2Br$, (c) $CsPbIBr_2$, and (d) $CsPbBr_3$. 2D Young's modulus: (e) $CsPbI_3$, (f) $CsPbI_2Br$, (g) $CsPbIBr_2$, and (h) $CsPbBr_3$. Reproduced with permission from ref. 128. Copyright©2020, Wiley Online Library.
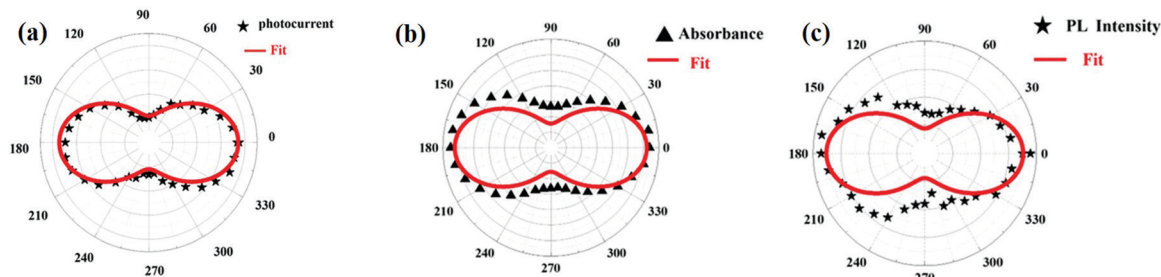
Fig. 9 The polarization dependence polar plot of (a) absorption and (b) PL spectra for CsPbBr$_3$ film. Black triangles and stars represent the experimental data and solid red lines are fitted curves. (c) The polarization effect on current intensity (bias voltage is 5 V and light intensity is 60 mW cm^{-2}). Reproduced with permission from ref. 129. Copyright©2019, Wiley Online Library.
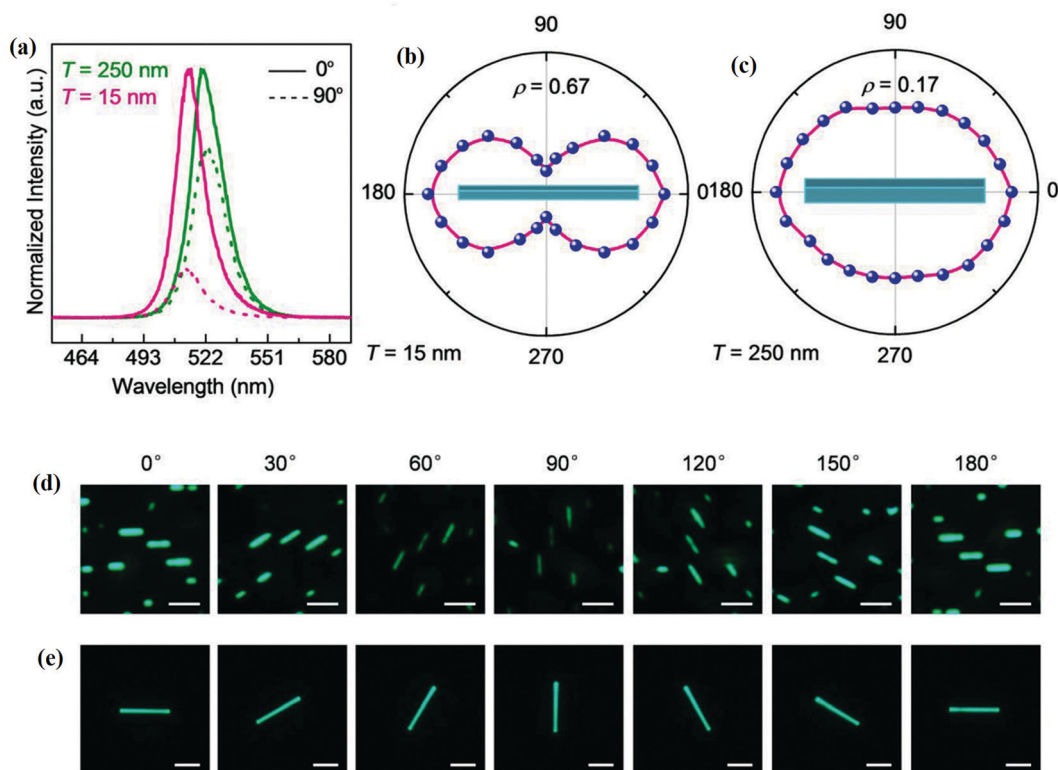

Fig. 10 (a) PL spectra; (b) and (c) polarization dependence PL intensity polar plots (polarization angle 0° represents the polarization field parallel to the NWs) of 15 nm and 250 nm NWs excited at 405 nm. The optical PL images of NWs at different polarization directions of NWs thickness (d) 15 nm (scale bar 250 nm), and (e) 250 nm (scale bar 3 μm). Reproduced with permission from ref. 130. Copyright©2018, Wiley Online Library.

3. Metal ion-doped CsPbX$_3$

All IHPs have been doped with different types of metal ions such as alkali metals, alkaline earth metals, transition and post-transition metals, and lanthanides. Among these metal cations, lanthanide doping is unique in the sense that they exhibit discrete emission in a wide spectral region ranging from the UV-visible to the near-infrared (NIR) region. These additional optical features bring multifunctionality to IHPs, particularly for emerging applications like NIR and white light-emitting diodes, NIR emitters, NIR cameras, optical temperature sensing, optical data encoding, *etc.* On the contrary, non-lanthanide metal doping only has been used to improve the existing applications, particularly for LEDs/WLEDs and solar cells. In this review, we have covered metal doping in IHPs in two different sections, *i.e.*, non-lanthanide metal-ion-doped IHPs (CsPbX$_3$) and lanthanide-ion-doped IHPs. However, the main focus is to highlight the effect of lanthanide doping in more detail.

3.1 Non-lanthanide metal ion-doped CsPbX$_3$

Metal ions (M-ion), other than lanthanides, such as alkali metal cations Li$^+$,[131] Na$^+$,[132] K$^+$,[133,134] and Rb$^+$,[135] alkaline earth metal cations Mg^{2+},[136] and Ca^{2+},[137] transition metals Zn^{2+},[138,139] Mn^{2+},[140–143] Ni^{2+},[144,145] Cu^{2+},[146,147] Ti^{3+},[148,149] Y^{3+},[150] and

3658 | *J. Mater. Chem. C*, 2022, **10**, 3647–3676

This journal is © The Royal Society of Chemistry 2022

Cd^{2+},[124] post-transition metal Sn^{2+},[151] *etc.*, have also been incorporated with the all-IHPs. These metal ions also improve the optoelectronic properties and the stability of IHPs against various environments. The alkali metal cations doped into the all-IHPs take the A-sites, *i.e.*, the Cs^+ position, whereas the alkaline earth metal cations, transition metals, and post transition metals take the B-site *i.e.*, the Pb^{2+} position. B-site doping largely affects the optoelectronic properties as compared to A-site doping.[152] The Mn^{2+} doping in place of Pb^{2+} into the $CsPbX_3$ reduces the toxicity and increases the PLQYs and stability. As explained, the α-$CsPbI_3$ perovskite, which shows good optoelectronic behavior, is unstable and is most likely to transform into the non-perovskite phase δ-$CsPbI_3$ having poor optoelectronic properties. Mn^{2+} doped into $CsPbI_3$ NCs stabilizes the α-$CsPbI_3$ phase.[153] It also improves the stability against UV irradiation as compared to the undoped $CsPbI_3$ NCs. It exhibits band edge excitonic d-d transitions and results in orange luminescence bands. However, Mn^{2+}-ion incorporation gives new emission bands, which result in impure light emission that limits practical applications. Sn^{2+} also takes the Pb^{2+} site and is less toxic than Pb^{2+}; however, Sn^{2+} is highly unstable and is oxidized to Sn^{4+}.

3.1.1 The effects of metal (non-lanthanide) doping on the optical properties of CsPBX$_3$

3.1.1.1 Alkali metal ion-doped CsPbX$_3$. The alkali metal ions such as Li^+,[131] Na^+,[132] K^+,[133,134] Rb^+,[135] *etc.*, have been doped in $CsPbX_3$ to improve the PLQYs. The alkali metal ion takes the Cs^+ position instead of Pb^{2+}. The doping concentration of alkali metal ion in $CsPbX_3$ improves the PLQYs up to a certain concentration limit, after which the PLQYs decreases. The average lifetime also varies in the same fashion as PLQYs with the doping of alkali metal ions in different concentrations. The PLQYs and the average lifetime of 1%Na:$CsPbCl_3$ QDs are 56.8% and 26.5 ns, respectively.[132] Both the PLQYs and the lifetime values gradually increase up to a doping of 4% Na ions and the maximum values are attained at 4% Na doping, *i.e.*, 94.2% and 32.2 ns, respectively. Beyond 4% doping concentration of Na, the PLQYs and average lifetime both decrease and the values dropped to 50.4% and 13.1 ns, respectively for 7%Na:$CsPbCl_3$ QDs. Similarly, the optimized doping concentration for Rb^+ ions was 9% in $CsPbCl_3$ for the maximum PLQYs and average lifetime.

3.1.1.2 Alkaline earth metal ion-doped CsPbX$_3$. The alkaline earth metal ions are among the dopants for all-IHPs, which are used to improve the optoelectronic properties of the pristine samples. Alkaline earth metal cations take the Pb^{2+} position instead of Cs^+, and have a large influence on the optoelectronic properties as compared to alkali metal ions that take the Cs^+ position.[152] Chen *et al.*[154] reported that there was no shift in the diffraction peaks for Mg^{2+}, Ca^{2+} and Sr^{2+}-doped $CsPbCl_3$ NCs as compared to pristine $CsPbCl_3$ NCs, which confirmed that there is no structural change after doping. However, a slight shift in the diffraction peaks towards low angles for Ba^{2+}-doped $CsPbCl_3$ NCs was observed. Since the ionic radius of Ba^{2+} (1.35 Å) is larger than Pb^{2+} (1.19 Å), it is less probable that

Ba^{2+} can take the Pb^{2+} position. However, Chen *et al.*[154] confirmed experimentally and theoretically that Ba^{2+} can enter the core region of the lattice of NCs. Because of the large ionic radius, it produces more stress and lattice distortion and consequently, the diffraction peak shifts to lower angle as observed in the XRD pattern of Ba^{2+}–$CsPbCl_3$ NCs. The PLQYs of the Ca^{2+}-doped $CsPbBr_3$ NCs was higher as compared to the undoped sample.[137,154] The X-ray diffraction (XRD) pattern of pristine $CsPbX_3$ NCs and doped Ca^{2+}:$CsPbX_3$ NCs at different doping concentrations are shown in Fig. 11(a) and (b), respectively for X = Br, and X = Br_1I_2. Fig. 11(c) shows the PL spectra of pristine $CsPbBr_3$ NCs and doped Ca^{2+}:$CsPbBr_3$ NCs, whereas Fig. 11(d) represents PL spectra of both pristine $CsPbBr_1I_2$ NCs and doped Ca^{2+}:$CsPbBr_1I_2$ NCs. For the doping concentration of Ca^{2+}-ion up to 40%, the PLQYs of the $CsPbBr_3$ NCs as well as $CsPbBr_1I_2$ NCs increase with the concentration.[137] For example, the values were 37.9% and 72.3% for Ca^{2+}-ion doping concentrations of 10% and 40%, respectively in $CsPbBr_3$ NCs, whereas the values were 44.0% and 78.7%, respectively in $CsPbBr_1I_2$ NCs. Further, for the doping concentrations of Ca^{2+}-ion above 40%, a decrease in PLQYs was observed in both cases and values were 64.5% and 67.7%, respectively in $CsPbBr_3$ NCs and $CsPbBr_1I_2$ NCs for Ca^{2+}-ion concentration of 50%.

The same variation trend was also observed for the average lifetimes indicated in Fig. 11(e and f). The average lifetimes were 49.45 ns and 108.15 ns for Ca^{2+}-ion doping concentrations of 10% and 40%, respectively, in $CsPbBr_3$, whereas it was 80.07 ns and 146.25 ns, respectively in $CsPbBr_1I_2$. The doping concentration of Ca^{2+} ions above 40% showed a decrease in the average lifetime in both cases. The average lifetimes were 98.96 ns and 106.99 ns, respectively in $CsPbBr_3$ and $CsPbBr_1I_2$ for Ca^{2+} ion concentration of 50%. Thus, the PLQYs and average lifetimes are higher in $CsPbBr_1I_2$ as compared to $CsPbBr_3$ for the same doping concentration of Ca^{2+} ions. This result indicates that the PLQYs and average lifetime can be increased by the partial or complete substitution of Br or I in place of Cl in $CsPbCl_3$ NCs. The optimized Ca^{2+} doping concentration for the high PLQYs and average lifetime in the host $CsPbCl_3$ was 10.5%.[154] For the higher doping concentration, the PLQYs and average lifetime decreased in a similar way as discussed above. Similarly, the optimized doping percentage of Mg^{2+} in $CsPbCl_3$ was 37.9% at which the maximum PLQY value and average lifetime were observed and were 75.8% and 23.931 ns, respectively. For Mg^{2+} doping concentration higher than 75.8%, both the PLQYs and average lifetime decrease.[136]

3.1.1.3 Transition metal ion-doped CsPbX$_3$. Transition metals such as Zn^{2+},[138,139] Mn^{2+},[140-143] Ni^{2+},[144,145] Cu^{2+},[146,147] Cd^{2+}, Ti^{3+},[148,149] Y^{3+},[150] Cd^{2+},[124] *etc.*, have been used as dopant elements for all-IHPs. The Mn^{2+} ion has been widely used for improving the PLQYs and stability and to reduce the toxicity of Pb-based all-IHPs. The schematic representation of $Cs(Pb/Mn)Cl_3$ is shown in Fig. 12(a). The XRD patterns of Mn^{2+}–$CsPbCl_3$ QDs with different doping concentrations are shown in Fig. 12(b). Mn^{2+} doped into the $CsPbCl_3$ exhibited two emission peaks; a narrow emission peak at around 400 nm
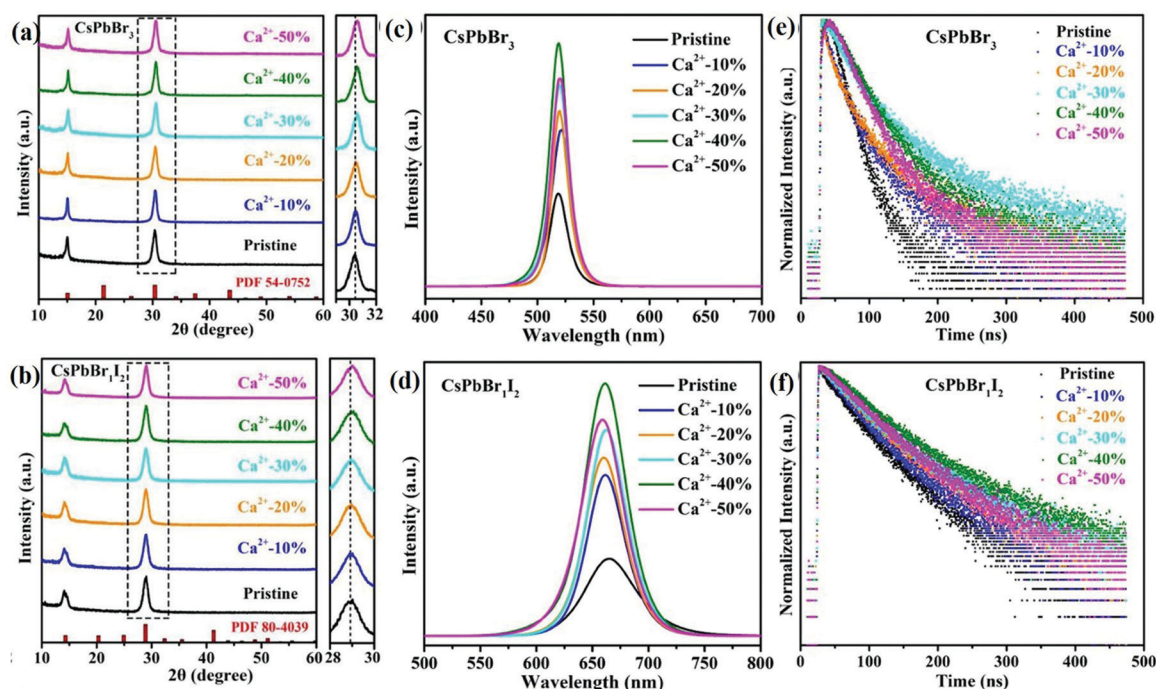
This journal is © The Royal Society of Chemistry 2022

J. Mater. Chem. C, 2022, **10**, 3647–3676 | **3659**

Fig. 11 XRD patterns of (a) pristine $CsPbBr_3$ NCs and Ca^{2+}–$CsPbBr_3$, (b) pristine $CsPbBr_1I_2$ NCs and Ca^{2+}–$CsPbBr_1I_2$ NCs with different Ca^{2+} concentrations (enlarged views of the peaks marked by the dotted outline are shown in the right panels). PL spectra of (c) pristine $CsPbBr_3$ NCs and Ca^{2+}–$CsPbBr_3$, (d) pristine $CsPbBr_1I_2$ NCs and Ca^{2+}–$CsPbBr_1I_2$ NCs. PL lifetimes of (e) pristine $CsPbBr_3$ NCs and Ca^{2+}–$CsPbBr_3$, (f) pristine $CsPbBr_1I_2$ NCs and Ca^{2+}–$CsPbBr_1I_2$ NCs. Reproduced with permission from ref. 137. Copyright©2021, Elsevier.

(due to exciton recombination) and a broad band emission at 600 nm by the Mn^{2+} intrinsic band edge transition as shown in Fig. 12(c).[140] These two peaks appeared at 460 nm and 610 nm for the Mn^{2+}–$CsPbBr_3$ nanoparticles.[155] The orange luminescence was observed at 600 nm in the PL spectra due to the spin-forbidden d–d transition in Mn^{2+}.[140,143] The intensities of the emission peaks at 406 nm and 600 nm can be tailored by the Mn^{2+} doping concentration.[140,156] For doping up to 20.4% Mn^{2+} (Mn : Pb = 2 : 5) in $CsPbCl_3$, the intensity corresponding to 406 nm was much higher as compared to the 600 nm emission peak as indicated in Fig. 12(c).[140] For 37.6% Mn^{2+} (Mn : Pb = 1 : 2) doping, both emission peaks showed comparable PL intensities. At higher doping concentrations, the intensity of the emission peak at 406 nm was significantly reduced,

whereas, the intensity of the emission peak at 600 nm increased.[140,156] The increase in the intensity of the 600 nm emission peak at higher doping concentration was due to the effective energy transfer from $CsPbCl_3$ to Mn^{2+}.[140] However, in the Mn^{2+}-doped $CsPbI_3$ NCs only one emission peak at 679 nm was reported and the peak position varied with the doping concentration.[153]

The PLQYs of the 5.0% Mn^{2+}-doped $CsPbI_3$ increased to 98%. To reduce the toxicity effect of Pb^{2+}, a high doping percentage of non-toxic metal is required. Taking toxicity into consideration, Guo et al.[139] reported the optimized doping of (Mn + Zn) into $CsPbBr_3$. On the basis of "t" and "μ" values within the structural stability limit, the maximum values of y and $(x + y)$ in $CsPb_{1-x-y}Mn_xZn_yBr_3$ were 25% and 83%,
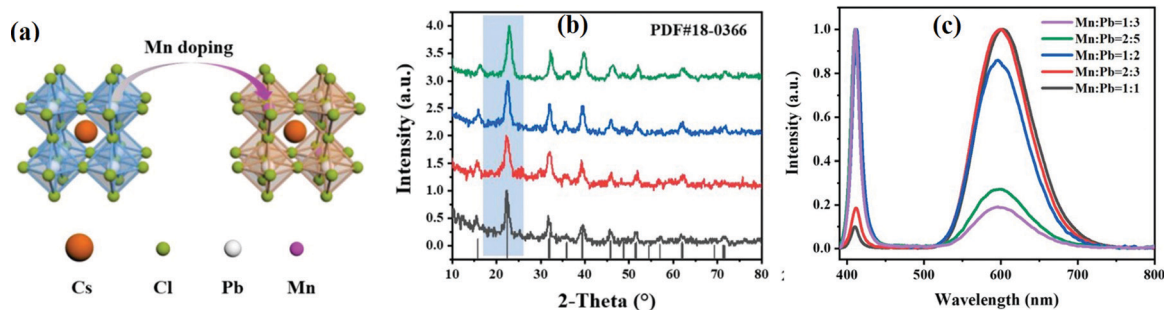

Fig. 12 (a) Schematic representation of $Cs(Pb/Mn)Cl_3$. (b) XRD pattern of the Mn^{2+}-doped $CsPbCl_3$ QD_S for Mn to Pb ratios of 1 : 3 (black), 2 : 5 (red), 1 : 2 (blue), 1 : 1 (green). (c) PL spectra of the Mn^{2+}:$CsPbCl_3$ QD_S prepared at different Mn:Pb ratios. Reproduced with permission from ref. 140. Copyright©2021, Elsevier.

respectively. However, (Mn + Zn) co-doping $(x + y)$ beyond 50% reduced the visible optical absorption, defect tolerance, and carrier lifetime. Therefore, the maximum doping percentage of (Mn + Zn) in $CsPb_{1-x-y}Mn_xZn_yBr_3$ was 50% without reducing the optoelectronic properties of the pristine $CsPbCl_3$ film. The Mn^{2+} co-doping with Cu^{2+} in $CsPbCl_3$ was also reported.[49] The Mn^{2+}–Cu^{2+} co-doped $CsPbCl_3$ NCs boosted the emission efficiency and 8% PLQYs was achieved.

3.1.1.4 Post transition metal ion-doped CsPbX$_3$. Post transition metal Sn^{2+} is also used as a dopant for all-IHPs.[151] A major issue with the Sn^{2+}-doped all-IHPs is related to its instability since it is readily oxidized to Sn^{4+}, which limits the practical application of Sn^{2+}-doped all-IHPs. However, researchers have adopted different synthesis approaches with different initial precursors to enhance the stability of Sn^{2+}-doped all-IHPs. The variation trend for the PLQYs and average lifetime with the Sn^{2+} doping concentration in all-IHPs is the same as for other metal doped all-IHPs. As reported by Yan *et al.*,[151] initially, the PLQYs and the average lifetime of the Sn^{2+}-doped $CsPbBr_3$ increased up to the doping concentration of 20% with maximum PLQYs and average lifetime values of 82.77% and 25.26 ns, respectively. For higher Sn^{2+}-doping concentrations, both values decreased. Table 5 summarizes the optoelectronic properties of non-lanthanide metal ion-doped all-IHPs at optimized doping concentrations. However, the listed optoelectronic values of doped $CsPbX_3$ are predominantly affected by the synthesis methods, precursors used for the synthesis, reaction temperature, reaction time, use of capping ligand, and the doping of different metal ions, *etc.*

3.1.2 Applications of non-lanthanide metal ion-doped CsPbX$_3$. Metal ion-doped all-IHPs have been used in various optoelectronic applications. Some widely explored application are for color LEDs,[136,138,140] and WLEDs,[137,141,150] *etc.* As usual, metal ion-doped all-IHPs have been explored for photovoltaic applications.[52]

Researchers have used various metal ion-doped all-IHPs for the fabrication of LEDs using various structural layers. The metal ion-doped LEDs were summarized in detail by Gao *et al.*[157] It was reported that Zn^{2+}-doped $CsPbI_3$ with the LED structure ITO/ZnO/PEI/Zn:CsPbI$_3$/TCTA/MoO$_3$/Au showed a external quantum efficiency of 15.1%.[158] The maximum luminescence described was 40 000 cd m^{-2} for the Na$^+$-doped $CsPbBr_3$ with ITO/PeDOT:PSS/perovskite/TPBi/LiF/Al LED structure.[159] Whereas, in the Mn^{2+}-doped $CsPbBr_3$, the maximum current efficiency of 6.41 cd A^{-1} was observed with layered structure ITO/PeDOT:PSS/poly-TPD/Mn:CsPbBr$_3$/TPBi/LiF/Al.[160]

WLEDs have been constructed mainly by combining non-lanthanide metal ion-doped $CsPbX_3$ with phosphor materials and LED chips. The CIE coordinates, luminescence efficiency (LE), color rendering index (CRI), and color temperature (CCT) of the non-lanthanide metal ion-doped $CsPbX_3$ are listed in Table 6.

Recently, Gao *et al.*[157] summarized metal ion-doped all-IHPs solar cells also consisting of different combinations of structural layers. Comparative analysis indicated that Ca^{2+}-doped $CsPbBr_1I_2$ had high solar cell parameter values with the solar cell structure FTO/TiO$_2$/Ca:CsPbBr$_1$I$_2$/spiro-OMeTAD/Au. The photo-conversion efficiency (PCE), short circuit current (J_{sc}), open-circuit voltage (V_{oc}) and fill factor (FF) of the FTO/TiO$_2$/Ca:CsPbBr$_1$I$_2$/spiro-OMeTAD/Au structure were 16.79%, 15.32 mA cm^{-2}, 1.32 V, and 83.29%, respectively.[52] Other metal ion-doped all-IHPs also showed significant results for solar cell applications, and can be improved by selecting the different structural layers.

3.2 Lanthanide-doped CsPbX$_3$: novel properties and emerging applications

3.2.1 Important aspects of lanthanide doping in CsPbX$_3$. Lanthanides have been widely explored as optically active dopants in inorganic crystal lattices, which are often insulating in nature.[163] The doping of trivalent lanthanides (Ln^{3+}) into traditional semiconductor nanocrystals is challenging because of their tetrahedral coordination. Interestingly, $CsPbX_3$ (X = Cl, Br, and I) perovskite nanocrystals provide the octahedral coordination suitable for Ln^{3+} doping. Over the last few years, tremendous success has been achieved in doping Ln^{3+} into $CsPbX_3$ nanocrystals, combining the excellent optoelectronic

Table 5 The optical and electronic properties of the metal (non-lanthanide)-doped all-inorganic halide perovskite (ABX$_3$)

Doping ion	M:CsPbX$_3$	Band gap (eV)	Emission peak (nm) (for λ_{exi} (nm))	Average lifetimes (ns)	Overall PLQYs (%)	Year
Li$^+$ (NA)	30.0%Li:CsPbBr$_3$ NCs	—	520	229.80	40.0	2021[131]
Na$^+$ (NA)	4.0%Ca:CsPbBr$_3$ QDs	—	514 (372)	32.20	94.2	2021[132]
K$^+$ (NA)	4.0%K:CsPbCl$_3$ QDs	3.05	410 (365)	12.98	10.3	2018[133]
Rb$^+$ (NA)	9.0%Rb:CsPbCl$_3$ QDs	3.05	407 (365)	10.20	13.0	2018[135]
Mg^{2+} (0.72 Å)	37.9%Mg:CsPbCl$_3$ NCs	3.084	401	23.931	75.8	2021[136]
Ca^{2+} (1.0 Å)	10.5%Ca:CsPbCl$_3$ NCs	—	407	17.86	77.1	2019[154]
	40.0%Ca:CsPbBr$_3$ NCs	—	520.9	108.15	72.3	2021[137]
	40.0%Ca:CsPbBr$_1$I$_2$ NCs	—	662.3	146.25	78.7	2021[137]
Cu^{2+} (0.73 Å)	2.32%Cu:CsPbCl$_3$ QDs	—	412 (365)	—	51.0	2021[147]
Mn^{2+} (0.97 Å)	37.6%Mn:CsPbCl$_3$ QDs	—	406, **600**	10.702	—	2021[140]
	x%Mn:CsPbBr$_3$ NPs	—	460, **610** (365)	21.66	64.4	2021[155]
	x%Mn:CsPb(Br/Cl)$_3$ QDs	—	463, **602** (365)	2.66	72.5	2021[141]
Ti^{3+} (0.67 Å)	9.67%Ti:CsPbCl$_3$ NCs	—	410	22.75	48.4	2021[149]
Ni^{2+} (0.69 Å)	11.9%Ni:CsPbCl$_3$ NCs	—	407	18.39	96.5	2018[144]
Cd^{2+} (0.93 Å)	x%Cd:CsPbCl$_3$ NCs	—	406 (375)	—	98.0	2018[124]
Sn^{2+} (NA)	30.0%Sn:CsPbBr$_3$ QDs	—	514	25.26	82.77	2021[151]

Table 6 WLED parameters of non-lanthanide metal ion-doped $CsPbX_3$

WLED structure	CIE coordinate	LE (lm W^{-1})	CRI	CCT (K)	Year
Li:CsPbBr$_3$ + Eu:BaMgAl$_{10}$O$_{17}$ + Eu:CaAlSiN$_3$	(0.3318, 0.3383)	—	—	5523	2021[131]
Y:CsPbBr$_1$I$_2$ + Ce:Y$_3$Al$_5$O$_{12}$ + InGaN LED chip	(0.34, 0.35)	61	83	—	2022[150]
Ca:CsPbBr$_1$I$_2$ + Ca:CsPbBr$_3$ + InGaN LED chip	(0.3366, 0.3376)	92.4	92.2	—	2022[137]
Mn:CsPb(Br/Cl)$_3$ + InGaN LED chip	(0.39, 0.38)	—	—	—	2021[141]
Ni:CsPbBr$_x$I$_{3-x}$ + Ce:YAG InGaN LED chip	(0.3621, 0.3458)	113.20	94.9	4336	2021[161]
Zn:CsPbBr$_3$ + Mn:K$_2$SiF$_6$ + blue LED chip	(0.327, 0.336)	36.0	—	5760	2021[162]
Sn:CsPbBr$_3$:AgInZnS:InGaN LED chip	(0.41, 0.48)	43.2	89	—	2021[151]

properties of the host with the f–f electronic transitions of the dopants. Charge neutrality, FRET pair formation, multifunctionality and emerging applications are the three major aspects that justify lanthanide doping in all-IHPs.

Charge neutrality consideration: at first the basic conditions that should be fulfilled while doping with another ion are charge neutrality and the size of the dopant. The charge neutrality condition is that the cationic and anionic charges should be the same for the charge balance. However, in some cases, the presence of excess charge is also beneficial for particular applications like solar cells for the charge transport layer. Concerning charge neutrality, lanthanides are remarkable candidates for substitution into the ABX_3 perovskite structure because of their comparable ionic radii with the Pb^{2+} ion (1.19 Å). Hence, in the doping process, the lanthanide replaces the Pb^{2+} ion because of its comparable ionic radius.[164] This could be confirmed experimentally by high-resolution XPS spectra. For example, the high-resolution XPS spectra indicated a decrease in the binding energy of Pb^{2+} $4f_{5/2}$, and Pb^{2+} $4f_{7/2}$ when Eu^{3+} ions were doped.[165] There was very little variation in the binding energies of Cs^{3+} $3d_{3/2}$, and Cs^{3+} $3d_{5/2}$. In Cl^- $2p_{1/2}$ and Cl^- $2p_{3/2}$, variation in binding energy was also very small. This indicates that Eu^{3+} ions occupy the Pb^{2+} lattice sites in the host lattice of $CsPbCl_3$ instead of Cs^+ and Cl^- sites.

Realization of FRET pairs: lanthanide-doped nanoparticles and IHPs QDs can make a FRET (fluorescence resonance energy transfer) pair. In this process, the lanthanide-doped NPs convert low-energy photons (e.g., IR-photons) into photons of high energy through the UC process.[166,167] These high energy photons are re-absorbed by the perovskite QDs through FRET and thereby, the electron and hole pairs are generated in the perovskite QDs. Finally, the emission of photons takes place from perovskite QDs through exciton recombination. Thus, the emission from perovskite QDs in principle can be achieved through IR excitation, which opens up a new area of applications.[58,167]

The FRET process in lanthanide-doped nanoparticles to perovskite QDs requires effective distance control between them, which is a difficult task. Further, the quenching of the upconversion (UC) luminescence intensity by QDs also depends on the absorbance coefficient of the perovskite QDs. Thus, the energy transfer efficiency (η_{ETE}) depends on both the position of the energy level and the effective distance between the emitter and the absorber.[58]

$$\eta^{ETE} = \frac{n_{abs}^{X}}{n_{em}^{Tm}} = \frac{I_0^{Tm} - I_X^{Tm}}{I_0^{Tm}} \tag{4}$$

I_0^{Tm} and I_X^{Tm} are the integrated intensities of the UCL of Tm^{3+} from the NPs in the absence and presence of $CsPbX_3$ perovskite QDs, respectively. The integrated intensity is measured with frequencies above the band edge of $CsPbX_3$. Zheng et al.[58] found that the energy transfer efficiency from LiYbF$_4$:0.5%Tm^{3+}@LiYF$_4$ core/shell NPs to perovskite QDs increased from 65.5 to 96.6 and 99.9% when the composition of the halide changed from Cl^- to Br^- and I^- ions, and are listed in Table 7. The energy transfer efficiency from the NPs to $CsPbCl_3$ is low. This may be due to the smaller UV absorbance in $CsPbCl_3$ as compared to the other $CsPbX_3$ perovskite QDs, as manifested by their absorption spectra. The UC quantum yields (UCQYs) under 980 nm CW diode laser excitation at a power density of 100 W cm^{-2} for pure LiYbF$_4$:0.5%Tm^{3+}@LiYF$_4$ core/shell NPs and NPs-sensitized $CsPbX_3$ perovskite QDs with varying halide compositions were studied. The overall UCQYs reported are (0.44 ± 0.07), (0.45 ± 0.10), and (0.36 ± 0.09)% for the chloride, bromide and iodide compositions in the perovskite QDs, respectively. This is indirectly proportional to the PLQYs of the PeQDs.

Multifunctionality and emerging applications: the halide perovskites were initially synthesized for perovskite-based solar

Table 7 Optical and electronic parameters of undoped and lanthanide ion-doped $CsPbCl_3$. Reproduced with permission from ref. 165. Copyright©2017, American Chemical Society

Doping ion	N/A	Ce^{3+}	Sm^{3+}	Eu^{3+}	Tb^{3+}	Dy^{3+}	Er^{3+}	Yb^{3+}
Ionic radius of dopant (Å)	N/A	1.034	0.964	0.950	0.923	0.881	0.908	0.858
Lattice constant (Å)	3.96	3.94	3.93	3.92	3.90	3.89	3.88	3.87
Absorption peak (nm)	400	395	390	392	390	382	381	375
Band gap (eV)	2.87	2.91	2.94	2.98	3.03	3.05	3.08	3.10
Excitation peak (nm) (for λ_{em} (nm))	368 (410)	385 (430)	470 (603)	360 (620)	400 (555)	372 (575)	400 (548)	390 (982)
Average lifetimes^a (ns)	4.1	3.7	6.2	6.7	7.1	7.6	8.2	9.1
Overall PLQYs (%)	3.8	24.3	14.1	27.2	31.2	27.6	15.1	142.7

^{a} Emission decay was monitored at 410 nm.

3662 | J. Mater. Chem. C, 2022, **10**, 3647–3676

This journal is © The Royal Society of Chemistry 2022

cells because of their exceptional optoelectronic properties leading to the high efficiency of solar cells.[168] The presence of volatile organic cations in the structure, however, reduces its stability. Therefore, efforts have been made to increase their stability and also to explore these optoelectronic properties for some other novel applications. One of the approaches for making them multifunctional involves the incorporation of lanthanide ions into the perovskite structure.[169,170] This not only makes halide perovskite suitable for extended applications, but also increases their stability and improves the efficiency of solar cells.[123,171,172] Huang et al.[173] fabricated NIR light-emitting diodes by Yb^{3+}-doped $CsPbCl_3$ perovskite nanocrystals with excellent long-term stability. Zhang et al.[174] reported Yb^{3+}-doped $CsPbCl_3$ nanocrystals that emit strong NIR light at 986 nm and the Yb^{3+}/Er^{3+} co-doped $CsPbCl_3$ nanocrystal has emission at 1533 nm. The PL quantum yield also increased from 5% to 127.8% on doping 2% Yb^{3+}-into $CsPbCl_3$. This shows a high NIR output irradiance of 112 mW cm^{-2}@400 mA, which may have great potential in the future as a light source in night-vision cameras. The Eu^{3+} ion doped $CsPbI_2Br$ solar cell was reported by Chen et al.[99] Solar cell efficiency of 12% was achieved with good thermal stability. It was also reported that the Eu^{3+} ion doping into $CsPbI_2Br$ stabilized the γ-$CsPbI_2Br$ phase, which also increased the device performance. The $CsPbBr_3$ perovskite showed up-conversion phenomena by using $BaYF_5$ as a sensitizer.[167] The nano-composite of $CsPbI_3$ and $CaF_2:Yb^{3+}/Ho^{3+}$ showed both up-conversion and down-conversion behavior.[166] This can be used in dual-mode bio-imaging applications.[175] The newly emerging applications of lanthanide-doped all-IHPs are in improved solar cell applications (Section 3.2.4.1), the generation of WLEDs (Section 3.2.4.2), NIR-light emitters, NIR LEDs, and NIR cameras (Section 3.2.4.3), optical temperature sensing (Section 3.2.4.4), and as optical encoding material (Section 3.2.4.5).

3.2.2 The effects of lanthanide doping on the stability and structure of $CsPbX_3$.

Lanthanide ion doping into halide perovskites not only brings multiple functionalities but also improves their environmental, thermal- and photo-stability, which have been major concerns for various optoelectronic device applications of all-IHPs. Various mechanisms explain the increase in the stability of the halide perovskites in the presence of lanthanide ions:[176] (i) lanthanide doping can affect the growth kinetics during the synthesis process and result in the formation of a stable perovskite phase.[177] (ii) In metal halide perovskites, $(Pb)^0$ and $(I)^0$ defects form, which work as recombination centers and also affect the life of the device. Wang et al.[178] demonstrated that the incorporation of the europium ion pair Eu^{3+}–Eu^{2+} can shuttle electrons and thereby recover the lead and iodide ions (Pb^{2+} and I^-). This simultaneously increases the efficiency and stability of the device. (iii) Apart from the lanthanide ion doping in halide perovskites, one can use lanthanide complexes, which are easily functionalized over halide perovskites surfaces, to improve the stability and multi-functionality. Chen et al.[172] have incorporated europium acetylacetonate $[Eu(Ac)_3]$ into the perovskite precursor $CsPbI_2Br$ and found that Eu^{3+} ions strongly interact with halide plumates. Some

amount of Eu^{3+} ions were also inserted into the interstices of the $CsPbI_2Br$ lattice, causing an increase in their crystal size and the remaining Eu^{3+} ions accumulated in the grain boundaries. This reduced the phase transformation of γ-$CsPbI_2Br$ to the non-perovskite phase and also increased its performance. (iv) Another mechanism could be the use of a layer of lanthanide complex before the halide perovskite, which can absorb the UV radiation and emit the characteristic emission of the lanthanide ions. In this way it can increase the device stability by masking the halide perovskite from UV light, and also the luminescence at a higher wavelength can be effectively used by halide perovskite. Duan et al.[171] monitored the photoconversion efficiency (PCE) of undoped and 3% Sm^{3+}-doped $CsPbBr_3$ for 60 days. It was found that under 0% relative humidity at 80 °C, the Sm^{3+}-doped $CsPbBr_3$ retained more than 90% of the initial PCE, whereas, for the undoped $CsPbBr_3$, the PCE retained only ~80% of the initial value. This revealed the improved thermal stability of the halide perovskite after lanthanide (Sm^{3+}) ion doping.

The I^--based halide perovskite showed phase transformation from the perovskite structure α to β then to γ and finally to the non-perovskite structure δ phase. Jena et al.[179] showed that the incorporation of Eu^{3+} ions stabilized the black α-$CsPbI_3$ phase with improved photovoltaic performance. Zhang et al.[174] reported that the $CsPbCl_3:Yb^{3+}$ NCs solution showed longer photostability than undoped $CsPbCl_3$ NCs. To demonstrate this, both samples were placed under the continuous irradiation of a 6 W UV (365 nm) lamp and the PL was recorded as a function of time. The undoped $CsPbCl_3$ NCs showed 80% decrease in PL intensity in 27 h, whereas, the same amount of decay in intensity was observed in 85 h for Yb^{3+}-doped $CsPbCl_3$ NCs. The lanthanide ions occupied the Pb^{2+} ion sites and also reduced the Cs^+ ion vacancies.[180] This in turn reduced the defect and trap states. Since the stability of halide perovskites and improving the efficiency of optoelectronic devices are still among the focus areas of research, further investigations on the integration of lanthanide ions with halide perovskites are expected to bring exciting outcomes.

3.2.3 The effects of lanthanide doping on the optical properties of $CsPbX_3$

3.2.3.1 The effects on UV-visible absorption and photoluminescence. The variation in the optical bandgap affects the band-to-band PL of semiconducting materials. The substitution of smaller ions (all lanthanides after Gd^{3+}) for the Pb^{2+} ion leads to lattice shrinkage. This causes an increased ligand field within the $[PbBr_6]^{4-}$ octahedra, leading to an increase in the bandgap. This effect can be monitored by recording the UV-visible absorption spectrum, which shows a shift in the absorption peak towards higher energy, i.e. a blue shift.[181] Lanthanide ion doping also increases the stability of the perovskite structure. The effects of lanthanide ion doping on the structural and optical properties in $CsPbCl_3$ were determined by Pan et al.[165] The XRD patterns of the pristine $CsPbCl_3$ NCs and Ln^{3+}-doped $CsPbCl_3$ NCs are shown in Fig. 13(a). These revealed that lanthanide ion doping preserves the structure of the host but the average crystallite size changes.[165] The average crystallite size decreases linearly towards the higher atomic number of lanthanide ions.[171] This also induces a blue

This journal is © The Royal Society of Chemistry 2022

J. Mater. Chem. C, 2022, **10**, 3647–3676 | **3663**

Fig. 13 (a) XRD patterns, (b) absorption spectrum, (c) emission spectra of pristine $CsPbCl_3$ NCs and lanthanide-doped $CsPbCl_3$ NCs. Reproduced with permission from ref. 165. Copyright©2017, American Chemical Society.

shift in the PL spectra, *i.e.*, an increase in the binding energy of the structure due to quantum confinements.[165,171,182] Fig. 13(b) shows that doping smaller-sized lanthanide ions into $CsPbCl_3$ resulted in the blue shift of the absorption edge.[165] This blue shift was also observed in the emission spectrum, indicating the increased bandgap of Ln^{3+}-doped $CsPbCl_3$ NCs. Table 7 summarizes the optoelectronic properties of the lanthanide-doped $CsPbCl_3$ NCs.

3.2.3.2 The effects on PL quantum yields and lifetimes. Lanthanide ion doping increases the PLQYs of $CsPbCl_3$.[165] In the lanthanide-doped $CsPbCl_3$ structure, defect modification takes place and results in increased PLQYs. It should be noted that the PLQYs of the Yb^{3+}-doped $CsPbCl_3$ crystal was much higher as compared to the other lanthanide dopants.[165,169] Zhou *et al.*[123] considered the different host compositions for lanthanide ion doping. Table 8 shows various combinations of host and lanthanide with their quantum yields, which might be useful in selecting a particular combination of the host and lanthanide. Among the different host and dopant combinations, high PLQY was observed for the Yb^{3+}–Pr^{3+}–Ce^{3+}-doped $CsPbCl_{3-x-y}Br_xI_y$, and a relatively low PLQY for Yb^{3+}–Dy^{3+}-doped $CsPbCl_{3-x-y}Br_xI_y$. The maximum and minimum PLQY were observed for Yb^{3+}–Pr^{3+}–Ce^{3+}-doped $CsPbClBr_2$ and Yb^{3+}–Dy^{3+}-doped $CsPbI_3$.

Time-resolved spectroscopy revealed that the lanthanide-doped $CsPbCl_3$ has a longer average lifetime than 1.8 ns for

undoped $CsPbCl_3$.[165] For Yb-doped $CsPbCl_3$ NCs the average lifetime is 22 ns, which is larger than undoped $CsPbCl_3$ NCs.[183] Pan *et al.*[182] reported that the average lifetime for 2.7%Ce: $CsPbCl_3$ was 5.3 ns. For 0.1% Dy-doped $CsPbBr_3$, the average lifetime was 27.88 ns, whereas for $CsPbBr_3$ it was 21.22 ns.[184] The average lifetime increased with Dy concentration and attained a maximum value 54.34 ns for 0.7% Dy-doped $CsPbBr_3$ and then decreased with further increase in the Dy concentrations to 42.26 ns for 0.9% Dy:$CsPbBr_3$. An initial increase in average lifetime indicates that the electronic defect-mediated non-radiative transition was effectively reduced due to Dy concentration. The decreased average lifetime at higher concentrations, *i.e.* at 0.9% Dy, was due to the concentration quenching effect of lanthanides. The average lifetime further increased with the higher atomic number of lanthanide ions for a particular $CsPbX_3$ host. Longer average lifetimes, as well as increased PLQYs, are the consequence of the partial elimination of non-radiative channels in the lanthanide-doped $CsPbCl_3$.

3.2.3.3 The effect of lanthanide doping concentration on the PL peak intensity of $CsPbX_3$. The PL peak intensity is a measure of the number of emitted photons. The intensity of PL spectra depends on various parameters such as the type of material, the local surrounding temperature and doping concentration, *etc.* Doping concentration-dependent PL studies of Eu^{3+}-doped

Table 8 The PLQYs (in %) of various lanthanide ion combinations in halide perovskite hosts. Reproduced with permission from ref. 123. Copyright©2019, American Chemical Society

	$CsPbCl_3$	$CsPbCl_{1.5}Br_{1.5}$	$CsPbClBr_2$	$CsPbBr_3$	$CsPbBr_2I$	$CsPbBrI_3$	$CsPbI_3$
Yb^{3+}	85	117	137	95	75	73	59
Yb^{3+}–Tb^{3+}	63	102	114	89	64	59	51
Yb^{3+}–Dy^{3+}	47	78	97	94	58	52	43
Yb^{3+}–Nd^{3+}	80	115	132	93	71	67	56
Yb^{3+}–Ce^{3+}	100	146	154	95	72	67	55
Yb^{3+}–Pr_{3+}	110	148	163	97	73	65	63
Yb^{3+}–Pr^{3+}–Ce^{3+}	118	153	173	95	79	72	65

3664 | *J. Mater. Chem. C*, 2022, **10**, 3647–3676

This journal is © The Royal Society of Chemistry 2022

$CsPbCl_3$ have been carried out by Pan *et al.*[92] The absorption edge and emission peak showed blue shifts with an increase in Eu^{3+} concentration as shown in Fig. 14. This blue shift is due to the lattice contraction with doping ion concentration.[165,169,185] Zhou *et al.*[169] confirmed that there was an increase in the bandgap with increasing the doping concentration. The intrinsic transition intensity corresponding to the Eu^{3+} ion increased with the doping concentration. This behavior is because the high doping concentration facilitates efficient energy transfer from the host $CsPbCl_3$ to Eu^{3+} ions. The PLQYs of the doped $CsPbCl_3$ initially increased and then decreased with the concentration of Eu^{3+} ions.[165] The maximum PL of Eu^{3+} appeared for the doping concentration of 7.8 mole% (see Fig. 14). The effect of a blue shift in the absorption and emission spectra was observed with the Lu^{3+}-doping concentration in Lu^{3+}-doped $CsPbBr_3$ NCs and in Yb^{3+}-doped $CsPbI_3$.[177,185] Hence, this trend may also be predicted for Ln^{3+}-doped $CsPbX_3$.

The optimized lanthanide doping concentration varies based on the $CsPbX_3$ host. Also, in the lanthanide-doped $CsPbX_3$, the PLQY and average lifetime initially increased with Ln^{3+}-doping concentration and attained a maximum value. The PLQYs and the average lifetime subsequently decreased for higher doping concentrations. The variation trend for optoelectronic properties like PLQYs, average lifetime, *etc.*, was the same as observed in the case of non-lanthanide metal ions-doped $CsPbX_3$.

3.2.4 Emerging applications of lanthanide-doped all-inorganic halide perovskites. The halide perovskites have continued to gain importance for photovoltaic and other optoelectronic devices since their inception. Initially, they were investigated for only photovoltaics but now all-IHPs are considered one of the best multifunctional materials. Over the last few years, researchers from the area of photovoltaics have been investigating lanthanide-doped all-IHPs because of their potential to increase the efficiency and the stability of the devices. In spite of photovoltaics and colored (visible and white) light-

emitting diode applications, the lanthanide-doped all-IHPs are being used in many new and emerging fields, which was not possible with undoped all-IHPs, particularly in the field of NIR emission, NIR LEDs, NIR cameras, optical encoding, luminescence-based sensing and non-linear emission processes, *etc.* In this section, we cover some specific applications that are due to the merit of lanthanide doping in CsPbX3 halide perovskites.

3.2.4.1 Advancements in solar cell application. To analyze the effects of lanthanide ion doping, Duan *et al.*[171] used lanthanide ions (Sm^{3+}, Tb^{3+}, Ho^{3+}, Er^{3+}, and Yb^{3+}) in $CsPbBr_3$ in the fabrication of solar cells and calculated different solar cell parameters. Table 9 summarizes the solar cell parameters for different devices that use lanthanide-doped all-IHPs. The data indicate that lanthanide doping significantly improves cell performance. They found an ultrahigh open-circuit voltage of $\sim$1.594 V under the one sun illumination for lanthanide ion-doped all-IHPs. The lanthanide doping also improved thermal stability. On exposure to 80% relative humidity in an air atmosphere, the efficiency of the solar cell remained almost unchanged over 110 days. The Ln-doped ABX_3 has been used as one of the layers of the solar cell structure, $FTO/c-TiO_2/m-TiO_2/Ln:CsPbX_3/carbon$. The results from Table 9 indicate the potential of lanthanide-doped all-IHPs materials for solar cell applications.

3.2.4.2 Lanthanide-doped all-inorganic halide perovskites for WLEDs. The halide perovskite QDs show a very high PL quantum yield, which allows various novel optoelectronic applications. One of their fascinating applications is in the fabrication of tunable colored LEDs. In recent years, lanthanide-doped all-IHPs have also been actively explored for this purpose. For example, Nd^{3+} doping into $CsPbBr_3$ NCs shifts the emission peak from 515 nm to 459 nm.[189] After the encapsulation of green light-emitting $CsPbBr_3$ NCs and blue-light emitting $CsPbBr_3:xNd^{3+}$ (x = 7.2%) NCs in the PMMA host and after
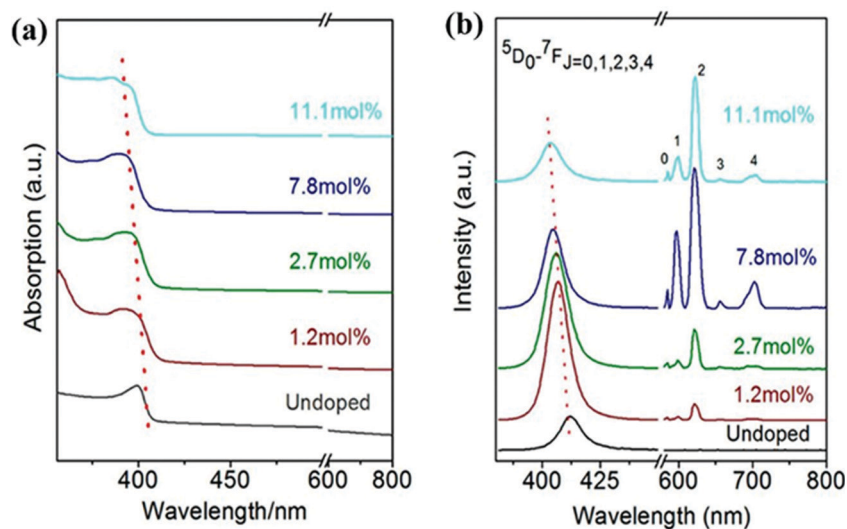

Fig. 14 (a) Absorption and (b) emission spectra under 365 nm excitation of $CsPbCl_3$ and different doping concentrations of Eu^{3+} in the $CsPbCl_3$ structure under 365 nm excitation. Reproduced with permission from ref. 165. Copyright©2017, American Chemical Society.

Table 9 Photovoltaic parameters of lanthanide-doped inorganic halide perovskites (characterization was done using solar simulator AM 1.5G with 100 mW cm^{-2} light intensity)

Halide perovskite	Dopant	Cell structure	J_{sc} (mA cm^{-2})	V_{oc} (V)	FF (%)	PCE (%)	Year
CsPbBr$_3$	Eu^{2+}	FTO/c-TiO$_2$/m-TiO$_2$/CsPb$_{1-x}$Eu$_x$Br$_3$/carbon	6.33	1.4523	79.19	7.28	2021[186]
CsPbBr$_3$	Yb^{3+}	FTO/c-TiO$_2$/m-TiO$_2$/CsPb$_{0.97}$Yb$_{0.03}$Br$_3$/carbon	7.45	1.536	80.20	9.20	2018[171]
CsPbBr$_3$	Er^{3+}	FTO/c-TiO$_2$/m-TiO$_2$/CsPb$_{0.97}$Er$_{0.03}$Br$_3$/carbon	7.46	1.563	82.80	9.66	2018[171]
CsPbBr$_3$	Ho^{3+}	FTO/c-TiO$_2$/m-TiO$_2$/CsPb$_{0.97}$Ho$_{0.03}$Br$_3$/carbon	7.45	1.572	83.20	9.75	2018[171]
CsPbBr$_3$	Tb^{3+}	FTO/c-TiO$_2$/m-TiO$_2$/CsPb$_{0.97}$Tb$_{0.03}$Br$_3$/carbon	7.47	1.588	84.80	10.06	2018[171]
CsPbBr$_3$	Sm^{3+}	FTO/c-TiO$_2$/m-TiO$_2$/CsPb$_{0.97}$Sm$_{0.03}$Br$_3$/carbon	7.48	1.594	85.10	10.14	2018[171]
CsPbI$_2$Br	Eu^{3+}	ITO/NiO/CsPb$_{0.995}$Eu$_{0.005}$I$_2$Br/PC$_{61}$BM/Ag	15.30	1.130	70.50	12.10	2021[172]
CsPbI$_2$Br	Eu^{3+}	FTO/c-TiO$_2$/m-TiO$_2$/CsPb$_{0.95}$Eu$_{0.05}$I$_2$Br/spiro-OMeTAD/Au	14.63	1.223	76.60	13.71	2019[187]
CsPbI$_3$	Eu^{3+}	FTO/TiO$_2$/CsPb$_{0.95}$Eu$_{0.05}$I$_3$/spiro-OMeTAD/Au	11.10	0.890	68.00	6.80	2018[179]
CsPbI$_3$	Yb^{3+}	FTO/TiO$_2$/CsPb$_{0.95}$Yb$_{0.05}$I$_3$/PTB7/MoO$_3$/Ag	13.25	1.250	75.00	12.42	2019[180]
CsPbI$_3$	Yb^{3+}	FTO/TiO$_2$/CsPbI$_3$:5%YbCl$_3$/spiro-OMeTAD/Ag	18.40	1.130	60.00	12.40	2020[188]

their deposition on a UV-LED having a red-emitting CsPbBr$_{1.2}$I$_{1.8}$/PMMA, WLEDs can be realized. The fabricated WLEDs have excellent color coordinates (0.34, 0.33) and NTSC value of 122% with a cool-white correlated color temperature of 5310 K. Yuan *et al.*[185] fabricated WLEDs by integrating Yb^{3+}-doped CsPbI$_3$ with the GaN LED blue-chip having the Y$_3$Al$_5$O$_{12}$:Ce^{3+} phosphor. The PL spectrum of Yb^{3+}-doped CsPbI$_3$ coated over GaN is shown in Fig. 15(a). The schematic of the WLEDs and color coordinates for WLEDs are shown in Fig. 15(b and c), respectively.

Pan *et al.*[182] compared the performance of WLEDs prepared using various lanthanide ion pairs in halide perovskites. They considered CsPbCl$_3$:2.7% Ce^{3+}:7.8% Eu^{3+}, CsPbCl$_{1.8}$Br$_{1.2}$:2.7% Ce^{3+}:7.8% Eu^{3+}, CsPbCl$_3$:2.7% Ce^{3+}:7.8% Sm^{3+} and CsPbCl$_{1.8}$Br$_{1.2}$: 2.7% Ce^{3+},7.8% Sm^{3+} for their studies. Among these four pairs, the maximum luminous efficiency (LE) and color rendering index (CRI) were 36 lm W^{-1} and 92, respectively for CsPbCl$_{1.8}$B$_1$r$_{.2}$:2.7% Ce^{3+}:7.8% Eu^{3+}. Zhu *et al.*[184] reported Dy^{3+}-doped CsPbBr$_3$ quantum dots to demonstrate WLEDs. For the generation of WLEDs, the green-emitting Dy^{3+}-doped CsPbBr$_3$ was incorporated with the red-emitting Mn^{2+}-doped K$_2$SiF$_6$ phosphor and blue-emitting InGaN chips. The CIE coordinates of the fabricated WLEDs reported were (0.2881, 0.3001) and the NTSC value was 126.3% on application of a 40 mA drive current. The Ce^{3+} ion incorporation into the CsPbCl$_3$ NCs enhanced the blue and green components.[182] It also behaved as a sensitizer for ions such as Eu^{3+} and Sm^{3+} and promoted red emission. This opens up future applications for WLED based on phosphor converted all-IHPs. Table 10

summarizes the lanthanide ion-doped CsPbX$_3$-based WLED parameters for the optimized lanthanide doping concentration.

3.2.4.3 Lanthanide-doped halide perovskites for NIR emission and NIR LEDs. All-IHPs are known for their characteristic emission in the visible region. Lanthanide doping adds some UV and infrared components of the electromagnetic spectrum due to 4f–4f transitions of different lanthanide ions. For example, the Yb^{3+}-doped CsPbBr$_3$ NCs showed NIR emission;[190] the NCs were encapsulated with SiO$_2$. The strong NIR (985) emission occurred from Yb^{3+} ions. This is the intrinsic luminescence of Yb^{3+} and is pumped by the perovskite host. The excitation and emission spectra of CsPbBr$_3$, Yb^{3+}-doped CsPbBr$_3$, and SiO$_2$-encapsulated Yb^{3+}-doped CsPbBr$_3$ NCs are shown in Fig. 16(a). The energy transfer process from the CsPbBr$_3$ to the Yb^{3+} ion is shown in Fig. 16(b).

The synthesized Yb^{3+}-doped CsPbBr$_3$ NCs emits strong NIR emission. The emission peak is centered at 985 nm. This originated from the $^2F_{5/2} \rightarrow {}^2F_{7/2}$ transition in Yb^{3+} ions. The intrinsic transition in Yb^{3+} ions is excited by efficient energy transfer from the perovskite host. Since there is a charge difference between Yb^{3+} and Pb^{2+}, the charge compensation defects Vpb were generated.[73,190] The Vpb exists between the two Yb^{3+} ions in the form of Yb^{3+}–Vpb–Yb^{3+}. The Vpb can excite two Yb^{3+} ions nearby through the quantum-cutting process and thus a high PL quantum yield is obtained.[191,192] The Yb^{3+}-doped CsPbCl$_3$ NCs emits 986 nm NIR light from the $^2F_{5/2} \rightarrow {}^2F_{7/2}$ transition, whereas Yb^{3+}/Er^{3+} co-doped CsPbCl$_3$ NCs emits

Fig. 15 (a) PL spectrum of Yb^{3+}-doped CsPbI$_3$ NCs integrated with the GaN blue chip. (b) Schematic of the device structure for WLEDs. (c) The color coordinates of the WLEDs (0.3499, 0.3542). Reproduced with permission from ref. 185. Copyright©2020, Elsevier.

3666 | *J. Mater. Chem. C*, 2022, **10**, 3647–3676

This journal is © The Royal Society of Chemistry 2022

Table 10 The lanthanide-doped CsPbX$_3$ WLEDs parameters

Ln-Doped WLED structure	CIE coordinates	LE (lm W^{-1})	CRI	CCT (K)	NTSC (%)	Year
Nd:CsPbBr$_3$ + CsPbBr$_3$ + CsPbBr$_{1.2}$I$_{1.8}$/PMMA film	(0.34, 0.33)	—	—	—	122.0	2020[189]
Dy:CsPbBr$_3$ + Mn:K$_2$SiF$_6$ + InGaN LED chip	(0.2881, 0.3001)	—	—	—	126.3	2022[184]
Yb:CsPbI$_3$ + Ce:Y$_3$Al$_5$O$_{12}$ + GaN LED chip	(0.3499, 0.3542)	57.3	85.4	3524	—	2020[185]
Ce:Eu:CsPbCl$_3$ + polystyrene + GaN LED chip	—	23	73	—	—	2018[182]
Ce:Eu:CsPbCl$_{1.8}$Br$_{1.2}$ + polystyrene + GaN LED chip	—	36	92	—	—	2018[182]
Ce:Sm:CsPbCl$_3$ + polystyrene + GaN LED chip	—	15	70	—	—	2018[182]
Ce:Sm:CsPbCl$_{1.8}$Br$_{1.2}$ + polystyrene + GaN LED chip	—	27	84	—	—	2018[182]

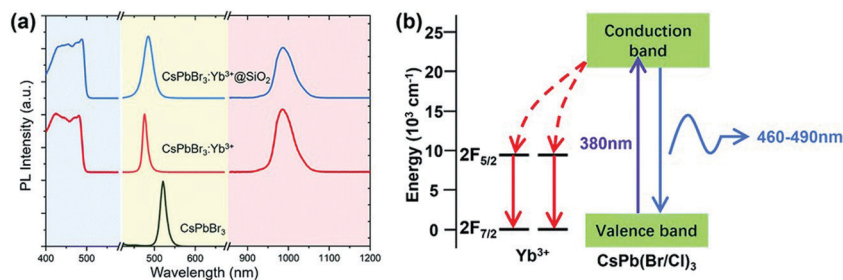**Fig. 16** (a) Excitation spectra (emission 985 nm, left), visible PL spectra (middle), and infrared PL spectra (right) of the synthesized CsPbBr$_3$, Yb^{3+}-doped CsPbBr$_3$, and SiO$_2$-encapsulated Yb^{3+}-doped CsPbBr$_3$ NCs. (b) Schematic diagram of energy transfer in the Yb^{3+}-doped CsPbBr$_3$ NCs. Reproduced with permission from ref. 190. Copyright©2020, Royal Society of Chemistry.

NIR emission centered at 1533 nm for the transition from $^4I_{13/2} \rightarrow {}^4I_{15/2}$ of Er^{3+} ions.[174] Zeng et al.[193] reported various strategies to enhance the NIR emission by doping lanthanide ions into the CsPbCl$_3$ NCs. It was observed that Er^{3+}, Ho^{3+}, and Nd^{3+} doping into CsPbCl$_3$ NCs can emit intense NIR light through energy transfer mediated by Mn^{2+} ions. The emission wavelength centered at 1542 nm was observed for Er^{3+} via a transition from $^4I_{13/2} \rightarrow {}^4I_{15/2}$. In Ho^{3+}, the transition takes place from $^5F_5 \rightarrow {}^5I_7$ and $^5F_5 \rightarrow {}^5I_6$ and corresponding emission peaks are observed at 986 nm and 1484 nm, respectively. In the case of Nd^{3+} ions, three emission peaks were observed which were centered at 888 nm, 1064 nm, and 1339 nm corresponding to $^4F_{3/2} \rightarrow {}^4I_{9/2}$, $^4F_{3/2} \rightarrow {}^4I_{11/2}$, and $^4F_{3/2} \rightarrow {}^4I_{13/2}$ transitions, respectively. Lanthanide-doped all-IHPs NIR emission transitions and their peak wavelengths are listed in Table 11.

NIR-LEDs are useful in night vision cameras, bio-imaging, communications and food processing industries. Huang et al.[173] proposed NIR-LEDs by doping ytterbium into CsPbCl$_3$. The emission and absorption spectra of CsPbCl$_3$ NCs and Yb^{3+} ion-doped CsPbCl$_3$ NCs are shown in Fig. 17. The emission of Yb^{3+} ions at ∼1000 nm is suitable for NIR-LEDs. Fig. 18 demonstrates the application of Yb^{3+}-doped CsPbCl$_3$ as a NIR camera. The device shows an output irradiance of 112 mW cm^{-2}@400 mA with

excellent stability. For the analysis of Yb^{3+}-doped CsPbCl$_3$ as a NIR camera, photographs of fruits and a fist were taken in natural light and phosphor-converted NIR-LED light. When the NIR-LED is off, the fruits and fist are invisible to the eye, whereas when the NIR-LED is on, the black and white images of the fruits and fist are observed. The images recorded under natural light phosphor-converted Yb^{3+}-doped CsPbCl$_3$ NIR-LED light are shown in Fig. 18(a) and (b), respectively.

3.2.4.4 Emerging applications for optical temperature sensing. In addition to the optoelectronic device applications, lanthanide-doped all-IHPs have recently been explored for various types of sensing applications. In recent years, temperature-dependent PL spectra have been studied widely in lanthanide-doped materials. Lanthanide-doped all-IHPs showed a linear variation in PL peak intensity with a temperature variation. This characteristic of Ln^{3+}-doped all-IHPs has attracted the attention of researchers for non-contact-based temperature sensing applications. In lanthanides and transition metals, the PL intensity variation occurs due to the electron population in the thermally coupled states.[194] However, a very small energy gap between these thermally coupled states leads to the overlapping of the emission. This affects the

Table 11 NIR emission in lanthanide-doped inorganic halide perovskites

Lanthanide-doped CsPbX$_3$	Transition	NIR emission peaks (nm)
Yb^{3+}–CsPbBr$_3$ NCs	$^2F_{5/2} \rightarrow {}^2F_{7/2}$	976,[173] 985,[190] 986[174]
Yb^{3+}/Er^{3+}–CsPbBr$_3$ NCs	$^4I_{13/2} \rightarrow {}^4I_{15/2}$ (Er^{3+})	1533[174]
Er^{3+}–CsPbCl$_3$ NCs	$^4I_{13/2} \rightarrow {}^4I_{15/2}$	1542[193]
Ho^{3+}–CsPbCl$_3$ NCs	$^5F_5 \rightarrow {}^5I_7$, $^5F_5 \rightarrow {}^5I_6$	986, 1484[193]
Nd^{3+}–CsPbCl$_3$ NCs	$^4F_{3/2} \rightarrow {}^4I_{9/2}$, $^4F_{3/2} \rightarrow {}^4I_{11/2}$, $^4F_{3/2} \rightarrow {}^4I_{13/2}$	888, 1064, 1339[193]
Yb^{3+}–CsPbI$_3$ QDs	$^2F_{5/2} \rightarrow {}^2F_{7/2}$	988[185]
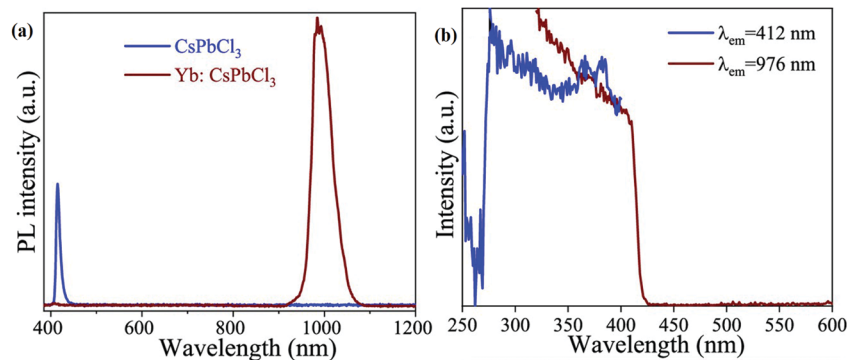
Fig. 17 (a) Emission and absorption spectra of CsPbCl$_3$ NCs and Yb^{3+}-doped CsPbCl$_3$ NCs. (b) Excitation spectra of CsPbCl$_3$ NCs and Yb^{3+}-doped CsPbCl$_3$ NCs. Reproduced with permission from ref. 173. Copyright©2021, American Chemical Society.
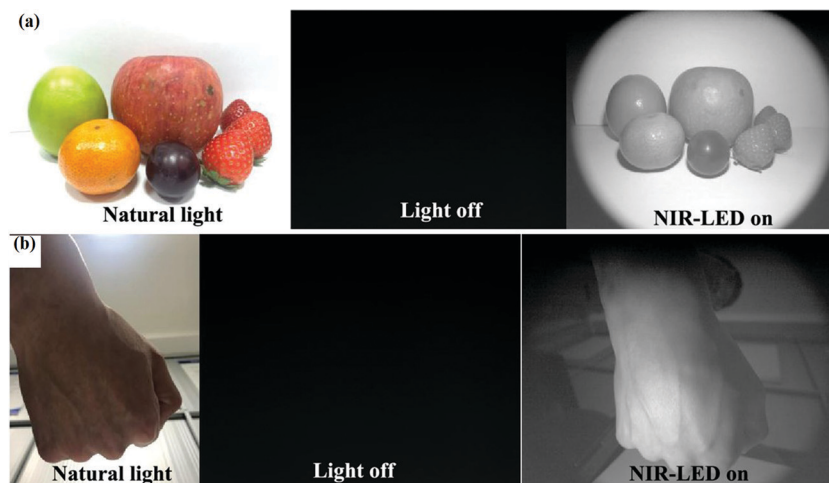

Fig. 18 Images of fruits and a fist under natural light and NIR-LEDs light were recorded using a visible and NIR camera, respectively. Reproduced with permission from ref. 173. Copyright©2021, American Chemical Society.

temperature sensing accuracy. With an increase in temperature, the electron–phonon coupling becomes more and more prominent and leads to the thermal quenching of the PL intensity.

Zhang *et al.*[195] demonstrated the application of Tb^{3+}-doped CsPbI$_3$ NCs for optical temperature sensing. The temperature-dependent emission spectra of Tb^{3+}-doped CsPbI$_3$ NCs are shown in Fig. 19(a). As the temperature increases, the emission intensities of both the Tb^{3+} ions and CsPbI$_3$ NCs decrease systematically. Fig. 19(b) shows the integrated emission intensities corresponding to Tb^{3+} and CsPbI$_3$ emission in Tb^{3+}-doped CsPbI$_3$ NCs at various temperatures. The fluorescence intensity ratio of Tb^{3+} at 544 nm and CsPbI$_3$ at 677 nm with excitation at 480 nm is given by the following:

$$\text{FIR} = \frac{I_{\text{Tb}}}{I_{\text{CPI}}} = \frac{I_{0,\text{Tb}}}{I_{0,\text{CPI}}} \frac{1 + A_{\text{CPI}} \exp\left(\frac{-E_{\text{CPI}}}{k_B T}\right)}{1 + A_{\text{Tb}} \exp\left(\frac{-E_{\text{Tb}}}{k_B T}\right)} \approx B + C \exp\left(\frac{-\Delta E}{k_B T}\right)$$

$$(5)$$

where I and I_0 are the PL intensities at temperature T and 0 K, respectively; A is a pre-exponential constant, T is the absolute temperature, the quenching activation energy is represented by E, and k_B is the Boltzmann constant. In the above equation, B, C and E are the values related to I_0, A and E, respectively.

The absolute sensitivity is defined as $S_A = \dfrac{\partial \text{FIR}}{\partial T}$, and the relative sensitivity is $S_R = \left|\dfrac{1}{\text{FIR}}\dfrac{\partial \text{FIR}}{\partial T}\right| \times 100\%$. The FIR value was calculated for the temperature range 80–480 K. The maximum reported values of S_A and S_R are 0.034 K^{-1} and 1.78% K^{-1} as shown in Fig. 19(c). The reversible effect on the FIR with temperature was also determined. The FIR remained almost the same in the cyclic temperature process as shown in Fig. 19(d). Yao *et al.*[196] also reported Dy:CsPbBr$_3$ QDs as a temperature sensor in the temperature range 80–298 K. For optimized Dy^{3+} doping, the Dy:CsPbBr$_3$ QDs showed the maximum relative sensitivity 2.39% K^{-1} at 298 K.

Table 12 summarizes the LED parameters of lanthanide-doped all-IHPs. Yb^{3+}-doped CsPbCl$_3$ showed a maximum S$_R$ of 3.31 K^{-1}, whereas the wide temperature range response of 80–480 K was observed in Tb^{3+}-doped CsPbCl$_3$. Therefore, one

3668 | *J. Mater. Chem. C*, 2022, **10**, 3647–3676

This journal is © The Royal Society of Chemistry 2022
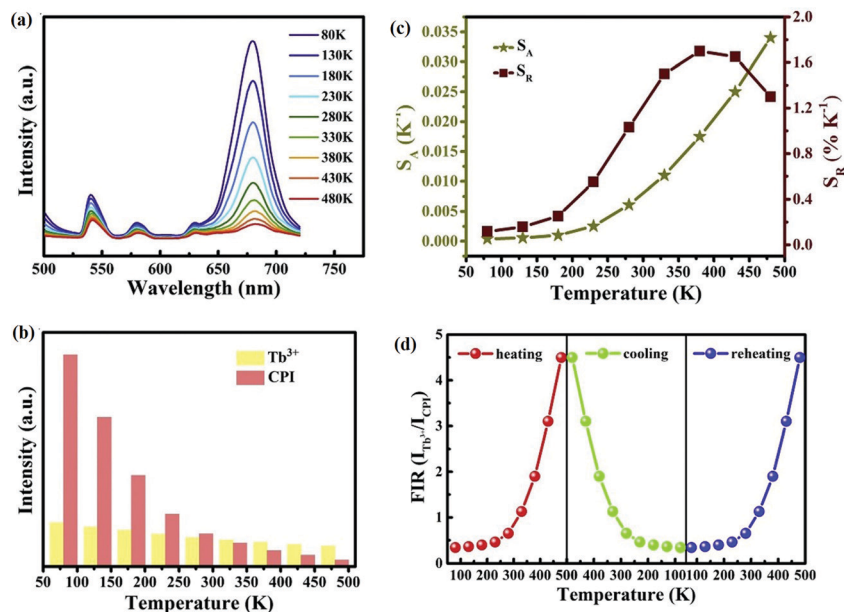
Fig. 19 (a) Temperature-dependent emission spectra of Tb^{3+}-doped $CsPbI_3$ NCs excited at 480 nm. (b) Integrated emission intensities corresponding to Tb^{3+} and $CsPbI_3$ emission in Tb^{3+}-doped $CsPbI_3$ NCs at various temperatures. (c) Absolute sensitivity S_A and relative sensitivity S_R versus T. (d) FIR in cyclic heating cooling and reheating. Reproduced with permission from ref. 195. Copyright©2020, Journal of European Ceramic Society.

Table 12 The thermometric parameters of Ln^{3+}-doped $CsPbX_3$ in temperature sensing

Ln^{3+}:$CsPbX_3$	Temperature range (K)	Maximum S_R (% K^{-1})	Maximum S_A (K^{-1})	Year
Tb:$CsPbI_3$ NCs	80–480	1.78	0.034	2020[195]
Dy:$CsPbBr_3$ QDs	80–298	2.39	—	2021[196]
Eu:$CsPbCl_2Br_1$ QDs	80–440	3.097	0.0315	2021[197]
Eu:$CsPbBr_3$ QDs	93–383	2.25	0.0224	2020[194]
Yb:$CsPbCl_3$	80–300	3.31	—	2021[73]

may select the particular combination of host and dopant to achieve the requirements under study. These open up future applications for fluorescence intensity ratio-based non-contact efficient temperature sensing. Hence, Ln^{3+} ion-doped $CsPbX_3$ shows prominent temperature sensitivity, which makes it a good candidate for temperature sensing applications.

3.2.4.5 Emerging application in optical encoding. In recent years, optical encoding research has become one of the most important fields of research in the scientific and technical industry for detecting counterfeiting. The poor materials, as well as their encoding in anti-counterfeiting technology, are easily depicted by the falsifier. It has been observed that stimuli-responsive fluorescence materials, such as lanthanide-doped all-IHPs, are very effective for optical data security with high recording density. Also, the fluorescence transitions switch between different states based on external factors such as temperature, dopant ions and their concentration, *etc.* Feng *et al.*[198] reported a novel approach to modeling optical encoding materials using europium complex-decorated $CsPbBr_3$ quantum dots with highly stable dual-stimuli-response. The schematic illustration of the formation of the europium complex Eu(PBA)₃AA (HPBA = *N*-(2pyridinyl)benzoylacetamide,

AA = 8-aminooctanoic acid)-decorated $CsPbBr_3$ quantum dots is shown in Fig. 20(a and b). The temperature and pH responses by the $CsPbBr_3$ (QDs) and Eu(PBA)₃AA, respectively, were observed in the luminescence spectra. This is useful for this application also. The encryption and decryption mechanisms are shown in Fig. 20(c) and (d), which show the dual responsive optical recording and encryption of the designed material.

OA/OAm-based QDs were painted on transfer paper and an encrypted word "LZU" was printed with Eu(PBA)₃AA-QDs, which was decoded only when the fluorescence of Eu(PBA)₃AA was enhanced by NH_3 vapor stimulation and the fluorescence of $CsPbBr_3$ was decreased by increasing the temperature to 80 °C as indicated in Fig. 20(d). The information "LZU" was doubly encrypted by temperature and pH and was readable only when these two values fulfilled the decryption conditions. Optical encryption and decryption were also reported by using Lu^{3+}-doped $CsPbBr_3$ but decryption occurred in UV light instead of NIR light.[177] The information "ZJU" was encrypted using the blue-emitting ink of Lu^{3+}:$CsPbBr_3$ on white paper. It is not possible to decode the information "ZJU" under daylight; however, when it encounters UV light of wavelength 360 nm, decryption of the information takes place. Hence, europium complex-decorated $CsPbBr_3$ quantum dots can be used as an optical encoding material in the future.
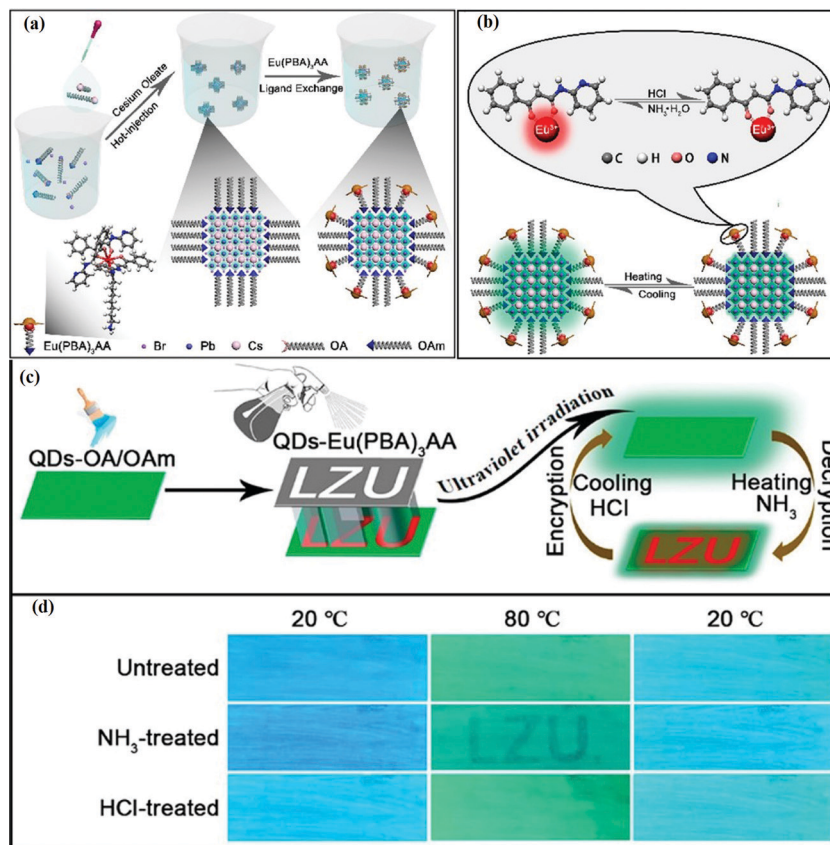
Fig. 20 (a) Schematic illustration of the formation of QDs–Eu(PBA)₃AA. (b) PL images of the dual-responsive optical recording and encryption. (c) The pattern design process and encryption and decryption mechanism. (d) PL images of patterns at different temperatures and pH. Reproduced with permission from ref. 198. Copyright©2021, American Chemical Society.

4. Summary and perspectives

The all-IHPs dominate organic–inorganic halide perovskites due to their better environmental stability, thus making them good candidates for optoelectronic applications. Conventionally, solid-state and liquid reaction synthesis methods have been used for the synthesis of bulk and nano-structured halide perovskites. Recently, researchers have reported several new synthesis techniques such as inject printing, spin coating, RF magnetron sputtering, single/multi crucible vacuum thermal evaporation, hot injection, *etc.* All these techniques have their advantages and disadvantages. Among these, the hot injection method is the most widely used method for the synthesis of all IHPs nanostructures with better stability. These reported synthesis methods are aimed toward the improved and stable structure of IHPs but none claim a completely stable phase synthesis. Therefore, the synthesis of cost-effective IHPs with long-term stability is still among the most challenging areas of research for IHPs.

In general, three phases (α, β, and γ) are observed in all-IHPs except in the perovskites formed by the halide I-atom, where an additional non-perovskite δ phase occurs. The cubic phase with a Goldschmidt tolerance factor value of 1 is the most stable structure. The stability can be increased by tailoring the Goldschmidt tolerance factor value by using surfactants and dopant

ions. One of the widely used dopants for IHPs is the lanthanide ion. The doping with lanthanide ions increases the stability (thermal stability, photostability, and phase stability) by reducing vacancies (defects and trap-states) in the structure and also improves optical properties. However, there is still a lot of scope for further improving the stability aspect of IHPs. A few frontline perspectives related to phase and stability issues can be outlined as follows. (i) Four phases are observed in all I-ion based IHPs. On heating, a direct transition from the α to δ phase occurs. However, in the cooling process, all four α, β, γ, and δ phases are observed. Herein, the reason for the direct transition from α to δ phase is not well addressed and needs further attention. (ii) Phase kinetics depends on both temperature and pressure. However, the study of applied pressure-based phase transition is not well explored in pristine and lanthanide-doped all-IHPs. (iii) In CsPbX₃, the toxicity of the Pb is unavoidable. Lead-free all-IHPs like CsGeX₃, CsGnX₃, *etc.*, are reported but their phase stability is quite low as compared to CsPbX₃. Replacing Pb²⁺ with any non-toxic cation considerably improves the stability and can open up an eco-friendly IHPs field. (iv) The development of single-crystal IHPs has not been tried so far. The single-crystal form of IHPs may also add new properties and should be explored in the future.

The all-IHPs provide a wide color gamut of emission spectra ranging from 400 nm to 700 nm by the compositional

3670 | *J. Mater. Chem. C*, 2022, **10**, 3647–3676

This journal is © The Royal Society of Chemistry 2022

management of halide ions. The FWHM of the emission peaks at 400 nm for $CsPbCl_3$ and 700 nm for $CsPbI_3$ ranges between 12 nm to 42 nm, respectively. The bandgap of the structure can be tailored from ~ 1.7 eV for $CsPbI_3$ to ~ 3.0 eV for $CsPbCl_3$. The doping of lanthanide ions in IHPs bestows them with excellent optical properties. It not only adds unique 4f–4f luminescence of lanthanide ions but affects the characteristic optical features of IHPs. The substitution of smaller-sized lanthanide ions (all lanthanide after Gd^{3+}) in place of Pb^{2+} ion leads to lattice shrinkage. This causes an increased ligand field within the $[PbBr_6]^{4-}$ octahedra, leading to an increase in the bandgap, and a blue shift in the PL is observed. Further, the emission intensity of the band-to-band transition of the host initially increases on increasing the lanthanide concentration because of the improved defect state, but after a certain limit, it starts decreasing due to FRET from the host to the doped lanthanide ion. Time-resolved spectroscopy reveals that the lanthanide-doped $CsPbX_3$ has a longer average lifetime and improved quantum yield as compared to the pristine $CsPbX_3$. In general, the average lifetime increases towards the higher atomic number of lanthanide ions. Longer average lifetimes, as well as increased PL quantum yields, are the consequences of the partial elimination of nonradiative channels in the lanthanide-doped $CsPbX_3$.

Anisotropic studies of Young's moduli of $CsPbI_3$, $CsPbBr_2I$, $CsPbBr_2I$ and $CsPbBr_3$ structures have been reported. Young's moduli of $CsPbI_3$ and $CsPbBr_3$ along different directions are the same, whereas $CsPbBrI_2$ showed isotropic nature along the [001] and [010] directions, and $CsPbBr_2I$ along the [100] and [010] directions. The anisotropic behaviors of $CsPbBrI_2$ and $CsPbBr_2I$ are reflected in almost all transport properties, except for bandgap energy. Although the anisotropy exists along the [001] and [100] directions for $CsPbBr_2I$ and $CsPbBrI_2$, respectively, the transport properties (electron and hole mobilities) are superior along [001] in both structures. In this direction, fewer carriers can be captured by the traps during transport. The superior properties of the crystal with the [001] orientation would be helpful in small devices for efficient output, such as transistors, light-emitting diodes, photodetectors, solar cells, etc. The extinction coefficients of $CsPbBr_2I$ and $CsPbBrI_2$ along the [001] direction are also greater as compared to [100] direction. Therefore, photon absorption along the [001] direction is greater and results in large current density and better spectral responsibility, which are required in optoelectronic applications. Thus, the anisotropic response for different parameters under applications is the extended field for making the device compact and with high efficiency. The effect of lanthanides on this property has not been explored so far.

Although optical properties have been widely explored, a few challenges remain. A theoretical understanding of various phenomena, such as phonon energy and its effect on optoelectronic properties and phase transition, the effect of temperature on PL spectra, in-depth study on doping ion behavior, etc., is still lacking and needs to be addressed. Similarly, the tuning of the emission peak width with narrow FWHM is also one of the important ignored aspects. Narrow-band emitting IHPs can be used for switching and lasing applications. In addition to this, lanthanide-doped IHPs can give multi-modal emission: downconversion, UC, and quantum-cutting luminescence. Such multimodal emission has not been explored well in IHPs. This multi-modal emission can be achieved by incorporating lanthanide-based phosphors/organic complexes in combination with the IHPs. This facilitates FRET pair formation between the duo, which opens up applications for biomedical imaging and sensing. However, such biological applications require lead-free and stable lanthanide-doped inorganic perovskites.

Due to the outstanding optoelectronic properties of all IHPs, they have attracted attention in several application areas like solar cells, colored LEDs, display devices, spectro-chemical probes, explosive detectors, laser fabrication, X-ray detection, etc. However, lanthanide doping has further extended its application fields and is additionally being used for WLEDs, NIR light emitters, NIR-LEDs, NIR cameras, temperature sensors, optical encoding, etc. For example, $Er^{3+}/Ho^{3+}/Nd^{3+}$-doping into $CsPbCl_3$ NCs gives intense NIR light through mediated energy transfer by Mn^{2+} ions. The IR emission centered at 1542 nm was observed with Er^{3+} doping. The doping of Ho^{3+} ions gave emission peaks at 986 nm and 1484 nm. Due to the doping of Nd^{3+} ions, three emission peaks were observed at 888 nm, 1064 nm, and 1339 nm. Similarly, the NIR emission at 980 nm from Yb^{3+}-doped $CsPbCl_3$ has been used for the development of NIR cameras, which could be useful in night vision surveillance, bio-imaging, communication and food processing industries, etc. In another application, Tb^{3+} ion-doped $CsPbI_3$ showed high-temperature sensitivity in the temperature range 80–480 K with the maximum values of absolute sensitivity (S_A) and relative sensitivity (S_R) 0.034 K^{-1} and 1.78% K^{-1}, respectively. Similarly, Eu complex-decorated $CsPbBr_3$ quantum dots have been used as an optical encoding material that has the potential for optical data storage and readout and anti-counterfeiting applications.

In conclusion, lanthanide doping not only improves the stability and optical properties of IHPs but also brings multifunctionality to them, beyond the well-established solar cell applications. Lanthanide-doped inorganic perovskites have great potential, and better theoretical and experimental studies may open up plenty of new application areas for them.

Conflicts of interest

There are no conflicts to declare.

References

1 H. Xiao, W. Dong, Y. Guo, Y. Wang, H. Zhong, Q. Li and M. Yang, *Adv. Mater.*, 2019, **31**, 1805802.

2 J.-S. Zhou, L. G. Marshall, Z.-Y. Li, X. Li and J.-M. He, *Phys. Rev. B*, 2020, **102**, 104420.

3 X. Zheng, L. Zhang, X. Wang, Y. Qing, J. Chen, Y. Wu, S. Deng, L. He, F. Liao and Y. Wang, *Inorg. Chem. Front.*, 2020, **7**, 3561–3570.

This journal is © The Royal Society of Chemistry 2022

J. Mater. Chem. C, 2022, **10**, 3647–3676 | **3671**

4 R. Russell, N. Ratcliff, K. Ahadi, L. Dong, S. Stemmer and J. W. Harter, *Phys. Rev. Mater.*, 2019, **3**, 91401.

5 B.-B. Zhang, X. Liu, B. Xiao, A. Ben Hafsia, K. Gao, Y. Xu, J. Zhou and Y. Chen, *J. Phys. Chem. Lett.*, 2019, **11**, 432–437.

6 F. Zhou, Z. Li, W. Lan, Q. Wang, L. Ding and Z. Jin, *Small Methods*, 2020, **4**, 2000506.

7 A. K. Singh, *Methods Appl. Fluoresc.*, 2020, **8**, 45008.

8 J. Wang, J. Zhang, Y. Zhou, H. Liu, Q. Xue, X. Li, C.-C. Chueh, H.-L. Yip, Z. Zhu and A. K. Y. Jen, *Nat. Commun.*, 2020, **11**, 1–9.

9 X. Gao, Q. Wang, Y. Zhang, C. Cui, N. Sui, X. Chi, H. Zhang, Q. Zhou, Y. Bao and Y. Wang, *J. Phys. Chem. C*, 2020, **124**, 11239–11247.

10 Z. Li, F. Zhou, Q. Wang, L. Ding and Z. Jin, *Nano Energy*, 2020, **71**, 104634.

11 A. Kojima, K. Teshima, Y. Shirai and T. Miyasaka, *J. Am. Chem. Soc.*, 2009, **131**, 6050–6051.

12 J. Ma, H. Wu, J. Qiu, J. Wang, Q. Wang, Y. Yang, D. Zhou and J. Han, *J. Mater. Chem. C*, 2019, **7**, 3751–3755.

13 J. Dong, D. Song, J. Meng, Y. Lu, Y. Li, B. Qiao, S. Zhao and Z. Xu, *J. Mater. Chem. C*, 2020, **8**, 6743–6748.

14 D. Yang and D. Huo, *J. Mater. Chem. C*, 2020, **8**, 6640–6653.

15 Y. Xu, S. Lou, C. Xia, T. Xuan and H. Li, *J. Lumin.*, 2020, **222**, 117132.

16 T. Wang, X. Wei, Y. Zong, S. Zhang and W. Guan, *J. Mater. Chem. C*, 2020, **8**, 12196–12203.

17 W. Xing, Q. Yao, W. Zhu, H. Jiang, X. Zhang, Y. Ji, J. Shao, W. Xiong, B. Wang and B. Zhang, *Small*, 2021, **17**, 2102733.

18 E. Aznar, I. Sanchez-Alarcon, P. J. R. Cantó, F. Perez-Pla, J. P. Martínez-Pastor and R. Abargues, *J. Mater. Chem. C*, 2022, **10**, 1754–1766.

19 Z. Wu, J. Yang, X. Sun, Y. Wu, L. Wang, G. Meng, D. Kuang, X. Guo, W. Qu and B. Du, *Sens. Actuators, B*, 2021, **337**, 129772.

20 J. Zhou, L. Xie, X. Song, Z. Wang, C. Huo, Y. Xiong, Z. Cheng, Y. Wang, S. Zhang, X. Chen and H. Zeng, *J. Mater. Chem. C*, 2020, **8**, 12632–12637.

21 Y. Liu, P.-A. Chen and Y. Hu, *J. Mater. Chem. C*, 2020, **8**, 16691–16715.

22 P. Zhang, Y. Hua, X. Li, L. Zhang, L. Liu, R. Li, G. Zhang and X. Tao, *J. Mater. Chem. C*, 2021, **9**, 2840–2847.

23 Y. Lin, X. Zheng, Z. Shangguan, G. Chen, W. Huang, W. Guo, X. Fan, X. Yang, Z. Zhao and T. Wu, *J. Mater. Chem. C*, 2021, **9**, 12303–12313.

24 Z. Yang, M. Jiang, L. Guo, G. Hu, Y. Gu, J. Xi, Z. Huo, F. Li, S. Wang and C. Pan, *Nano Energy*, 2021, **85**, 105951.

25 V. O. Eze, G. R. Adams, L. Braga Carani, R. J. Simpson and O. I. Okoli, *J. Phys. Chem. C*, 2020, **124**, 20643–20653.

26 M. I. Saleem, S. Yang, R. Zhi, M. Sulaman, P. V. Chandrasekar, Y. Jiang, Y. Tang, A. Batool and B. Zou, *Adv. Mater. Interfaces*, 2020, **7**, 1–7.

27 X. Chen, C. Sun, Y. Liu, L. Yu, K. Zhang, A. M. Asiri, H. M. Marwani, H. Tan, Y. Ai, X. Wang and S. Wang, *Chem. – Eng. J.*, 2020, **379**, 122360.

28 T. Masuda, Y. Zhang, C. Ding, F. Liu, K. Sasaki, Q. Shen and M. Endo, *J. Appl. Phys.*, 2020, **127**, 243104.

29 X. Wang, Y. Li, Y. Xu, Y. Pan, C. Zhu, D. Zhu, Y. Wu, G. Li, Q. Zhang, Q. Li, X. Zhang, J. Wu, J. Chen and W. Lei, *Chem. Mater.*, 2020, **32**, 4973–4983.

30 B. Bin Zhang, X. Liu, B. Xiao, A. Ben Hafsia, K. Gao, Y. Xu, J. Zhou and Y. Chen, *J. Phys. Chem. Lett.*, 2020, **11**, 432–437.

31 A. R. Chakhmouradian and P. M. Woodward, *Phys. Chem. Miner.*, 2014, **41**, 387–391.

32 Z. Yi, N. H. Ladi, X. Shai, H. Li, Y. Shen and M. Wang, *Nanoscale Adv.*, 2019, **1**, 1276–1289.

33 V. M. Goldschmidt, *Naturwissenschaften*, 1926, **14**, 477–485.

34 A. K. Singh, S. Singh, V. N. Singh, G. Gupta and B. K. Gupta, *J. Colloid Interface Sci.*, 2019, **554**, 668–673.

35 H. Wang, J. Lin, Y. Zhu, X. Zeng, H. Wei, P. Cheng, H. Lu, Y. Liu and R. Xiong, *Adv. Electron. Mater.*, 2020, **6**, 1–7.

36 S. M. Shakouri, E. Bagherzadeh-Khajehmarjan and S. Ahmadi-Kandjani, *Phys. Scr.*, 2019, **94**, 55503.

37 E. Bagherzadeh-Khajehmarjan, S. Mirershadi and S. Ahmadi-Kandjani, *Appl. Phys. B*, 2017, **123**, 1–6.

38 L. Guo, G. Tang and J. Hong, *Chinese Phys. Lett.*, 2019, **36**, 56201.

39 S. Yang, L. Wang, L. Gao, J. Cao, Q. Han, F. Yu, Y. Kamata, C. Zhang, M. Fan, G. Wei and T. Ma, *ACS Appl. Mater. Interfaces*, 2020, **12**, 13931–13940.

40 M. Tyunina, L. L. Rusevich, E. A. Kotomin, O. Pacherova, T. Kocourek and A. Dejneka, *J. Mater. Chem. C*, 2021, **9**, 1693–1700.

41 D. Hu, J. Dong, J. Tian, W. Wang, Q. Wang, Y. Xue, X. Xu and J. Xu, *J. Lumin.*, 2021, 118243.

42 Z. He, P. Yu, H. Wang, J. Gao, Y. Zhao, H. Zhang, Y. Zhao and Z. Miao, *J. Am. Ceram. Soc.*, 2021, **104**, 4389–4397.

43 A. Mahapatra, D. Prochowicz, J. Kruszyńska, S. Satapathi, S. Akin, H. Kumari, P. Kumar, Z. Fazel, M. M. Tavakoli and P. Yadav, *J. Mater. Chem. C*, 2021, **9**, 15189–15200.

44 Y. Chen, S. Tao, Y. Liu, X. Fu, M. Pei, X. Hou, H. Zhou, J. Yin and X. Zhang, *J. Nanoelectron. Optoelectron.*, 2021, **16**, 707–714.

45 Z. Irshad, M. Adnan and J. K. Lee, *J. Phys. Chem. Solids*, 2022, **160**, 110374.

46 M. W. A. Sektiono, F. A. Permatasari, A. H. Aimon and F. Iskandar, *RSC Adv.*, 2021, **11**, 1360–1366.

47 X. Zhang, B.-B. Zhang, X. Ma, M. Fu, G. Zha and W. Jie, *J. Phys. Chem. C*, 2021, **125**, 13033–13040.

48 V.-A. Ha, G. Volonakis, H. Lee, M. Zacharias and F. Giustino, *J. Phys. Chem. C*, 2021, **125**, 21689–21700.

49 R. Chakraborty, A. Maiti, U. K. Ghorai and A. J. Pal, *ACS Appl. Nano Mater.*, 2021, **4**, 10155–10163.

50 K. Enomoto, R. Oizumi, N. Aizawa, T. Chiba and Y.-J. Pu, *J. Phys. Chem. C*, 2021, **125**, 19368–19373.

51 R. Han, Q. Zhao, J. Su, X. Zhou, X. Ye, X. Liang, J. Li, H. Cai, J. Ni and J. Zhang, *J. Phys. Chem. C*, 2021, **125**, 8469–8478.

52 Y. Han, H. Zhao, C. Duan, S. Yang, Z. Yang, Z. Liu and S. Liu, *Adv. Funct. Mater.*, 2020, **30**, 1909972.

53 C. Quan, X. Xing, S. Huang, M. Jin, T. Shi, Z. Zhang, W. Xiang, Z. Wang and Y. Leng, *Photonics Res.*, 2021, **9**, 1767–1774.

54 E. J. Juarez-Perez, Z. Hawash, S. R. Raga, L. K. Ono and Y. Qi, *Energy Environ. Sci.*, 2016, **9**, 3406–3410.

3672 | *J. Mater. Chem. C*, 2022, **10**, 3647–3676

This journal is © The Royal Society of Chemistry 2022

55 C. C. Boyd, R. Cheacharoen, T. Leijtens and M. D. McGehee, *Chem. Rev.*, 2018, **119**, 3418–3451.

56 T. Ma, S. Wang, Y. Zhang, K. Zhang and L. Yi, *J. Mater. Sci.*, 2020, **55**, 464–479.

57 L. Protesescu, S. Yakunin, M. I. Bodnarchuk, F. Krieg, R. Caputo, C. H. Hendon, R. X. Yang, A. Walsh and M. V. Kovalenko, *Nano Lett.*, 2015, **15**, 3692–3696.

58 W. Zheng, P. Huang, Z. Gong, D. Tu, J. Xu, Q. Zou, R. Li, W. You, J. C. G. Bünzli and X. Chen, *Nat. Commun.*, 2018, **9**, 1–9.

59 L. Chen, Y. Chuang, W.-D. Yang, K.-C. Tsai, C.-W. Chen and C.-D. Dong, *J. Alloys Compd.*, 2021, **856**, 157426.

60 W. Zhao, R. Su, Y. Huang, J. Wu, C. F. Fong, J. Feng and Q. Xiong, *Nat. Commun.*, 2020, **11**, 1–7.

61 H. Näsström, P. Becker, J. A. Márquez, O. Shargaieva, R. Mainz, E. Unger and T. Unold, *J. Mater. Chem. A*, 2020, **8**, 22626–22631.

62 J. Li, R. Gao, F. Gao, J. Lei, H. Wang, X. Wu, J. Li, H. Liu, X. Hua and S. F. Liu, *J. Alloys Compd.*, 2020, **818**, 152903.

63 C. Borri, N. Calisi, E. Galvanetto, N. Falsini, F. Biccari, A. Vinattieri, G. Cucinotta and S. Caporali, *Nanomaterials*, 2020, **10**, 1–11.

64 H. Zhang, X. Fu, Y. Tang, H. Wang, C. Zhang, W. W. Yu, X. Wang, Y. Zhang and M. Xiao, *Nat. Commun.*, 2019, **10**, 1–8.

65 F. Liu, Y. Zhang, C. Ding, S. Kobayashi, T. Izuishi, N. Nakazawa, T. Toyoda, T. Ohta, S. Hayase, T. Minemoto, K. Yoshino, S. Dai and Q. Shen, *ACS Nano*, 2017, **11**, 10373–10383.

66 L. Bai, S. Wang, Y. Zhang, K. Zhang, H. Li, K. Ou and L. Yi, *J. Lumin.*, 2020, **226**, 117422.

67 Y. Li, X. Wang, W. Xue, W. Wang, W. Zhu and L. Zhao, *Nano Res.*, 2019, **12**, 785–789.

68 R. X. Yang, J. M. Skelton, E. L. Da Silva, J. M. Frost and A. Walsh, *J. Chem. Phys.*, 2020, **152**, 24703.

69 R. L. Armstrong, *J. Magn. Reson.*, 1975, **20**, 214–231.

70 S. Plesko, R. Kind and J. Roos, *J. Phys. Soc. Jpn.*, 1978, **45**, 553–557.

71 M. I. Cohen, K. F. Young, T. Chang and W. S. Brower Jr, *J. Appl. Phys.*, 1971, **42**, 5267–5272.

72 S. Hirotsu, *J. Phys. Soc. Jpn.*, 1971, **31**, 552–560.

73 M. Stefanski, M. Ptak, A. Sieradzki and W. Strek, *Chem. Eng. J.*, 2021, **408**, 127347.

74 X. Zhang, F. Wang, B. Bin Zhang, G. Zha and W. Jie, *Cryst. Growth Des.*, 2020, **20**, 4585–4592.

75 S. Hirotsu, J. Harada, M. Iizumi and K. Gesi, *J. Phys. Soc. Jpn.*, 1974, **37**, 1393–1398.

76 D. Malyshkin, V. Sereda, I. Ivanov, M. Mazurin, A. Sednev-Lugovets, D. Tsvetkov and A. Zuev, *Mater. Lett.*, 2020, **278**, 128458.

77 M. Rodová, J. Brožek, K. Knížek and K. Nitsch, *J. Therm. Anal. Calorim.*, 2003, **71**, 667–673.

78 Š. Svirskas, S. Balčiūnas, M. Šimėnas, G. Usevičius, M. Kinka, M. Velička, D. Kubicki, M. E. Castillo, A. Karabanov and V. V. Shvartsman, *J. Mater. Chem. A*, 2020, **8**, 14015–14022.

79 A. Marronnier, G. Roma, S. Boyer-Richard, L. Pedesseau, J. M. Jancu, Y. Bonnassieux, C. Katan, C. C. Stoumpos, M. G. Kanatzidis and J. Even, *ACS Nano*, 2018, **12**, 3477–3486.

80 M. Lai, Q. Kong, C. G. Bischak, Y. Yu, L. Dou, S. W. Eaton, N. S. Ginsberg and P. Yang, *Nano Res.*, 2017, **10**, 1107–1114.

81 J.-K. Sun, S. Huang, X.-Z. Liu, Q. Xu, Q.-H. Zhang, W.-J. Jiang, D.-J. Xue, J.-C. Xu, J.-Y. Ma and J. Ding, *J. Am. Chem. Soc.*, 2018, **140**, 11705–11715.

82 B. Zhao, S. F. Jin, S. Huang, N. Liu, J. Y. Ma, D. J. Xue, Q. Han, J. Ding, Q. Q. Ge, Y. Feng and J. S. Hu, *J. Am. Chem. Soc.*, 2018, **140**, 11716–11725.

83 Z. Yang, A. Surrente, K. Galkowski, A. Miyata, O. Portugall, R. J. Sutton, A. A. Haghighirad, H. J. Snaith, D. K. Maude, P. Plochocka and R. J. Nicholas, *ACS Energy Lett.*, 2017, **2**, 1621–1627.

84 W. Travis, E. N. K. Glover, H. Bronstein, D. O. Scanlon and R. G. Palgrave, *Chem. Sci.*, 2016, **7**, 4548–4556.

85 C. J. Bartel, C. Sutton, B. R. Goldsmith, R. Ouyang, C. B. Musgrave, L. M. Ghiringhelli and M. Scheffler, *Sci. Adv.*, 2019, **5**, eaav0693.

86 G. Wang, M. Lei, J. Liu, Q. He and W. Zhang, *Sol. RRL*, 2020, **4**, 1–20.

87 Y. Tang, A. Lesage and P. Schall, *J. Mater. Chem. C*, 2020, **8**, 17139–17156.

88 J. T. Matondo, D. M. Malouangou, L. Bai, Y. Yang, J. N. Ondze, T. Bimenyimana and M. Guli, *J. Mater. Chem. C*, 2021, **9**, 9377–9399.

89 F. Li and M. Liu, *J. Mater. Chem. A*, 2017, **5**, 15447–15459.

90 H. Peng, M. Cai, J. Zhou, Y. Yang, X. Ding, Y. Tao, G. Wu, X. Liu, J. H. Pan and S. Dai, *Sol. RRL*, 2020, **4**, 2000216.

91 C. Zhang, K. Wang, Y. Wang, W. S. Subhani, X. Jiang, S. Wang, H. Bao, L. Liu, L. Wan and S. Liu, *Sol. RRL*, 2020, **4**, 2000254.

92 J. Shi, F. Li, Y. Jin, C. Liu, B. Cohen-Kleinstein, S. Yuan, Y. Li, Z. Wang, J. Yuan and W. Ma, *Angew. Chem.*, 2020, **132**, 22414–22421.

93 N. Mondal and A. Samanta, *Nanoscale*, 2017, **9**, 1878–1885.

94 J. A. Steele, H. Jin, I. Dovgaliuk, R. F. Berger, T. Braeckevelt, H. Yuan, C. Martin, E. Solano, K. Lejaeghere, S. M. J. Rogge, C. Notebaert, W. Vandezande, K. P. F. Janssen, B. Goderis, E. Debroye, Y. K. Wang, Y. Dong, D. Ma, M. Saidaminov, H. Tan, Z. Lu, V. Dyadkin, D. Chernyshov, V. Van Speybroeck, E. H. Sargent, J. Hofkens and M. B. J. Roeffaers, *Science*, 2019, **365**, 679–684.

95 H. Lin, C. Zhou, Y. Tian, T. Siegrist and B. Ma, *ACS Energy Lett.*, 2017, **3**, 54–62.

96 H. Liu, Z. Wu, H. Gao, J. Shao, H. Zou, D. Yao, Y. Liu, H. Zhang and B. Yang, *ACS Appl. Mater. Interfaces*, 2017, **9**, 42919–42927.

97 G. Nedelcu, L. Protesescu, S. Yakunin, M. I. Bodnarchuk, M. J. Grotevent and M. V. Kovalenko, *Nano Lett.*, 2015, **15**, 5635–5640.

98 L. Yuan, Y. Zhou, Z. Wang, E. Mei, X. Liang and W. Xiang, *Appl. Clay Sci.*, 2021, **211**, 106158.

This journal is © The Royal Society of Chemistry 2022

J. Mater. Chem. C, 2022, **10**, 3647–3676 | **3673**

99 C. Gai, D. He, Y. Wang, J. Wang and J. Li, *Coatings*, 2021, **11**, 330.

100 J. Deng, J. Xun and R. He, *Opt. Mater.*, 2020, **99**, 109528.

101 A. Swarnkar, A. R. Marshall, E. M. Sanehira, B. D. Chernomordik, D. T. Moore, J. A. Christians, T. Chakrabarti and J. M. Luther, *Science*, 2016, **354**, 92–95.

102 Y. Dong, T. Qiao, D. Kim, D. Parobek, D. Rossi and D. H. Son, *Nano Lett.*, 2018, **18**, 3716–3722.

103 Q. Shang, A. L. Kaledin, Q. Li and T. Lian, *J. Chem. Phys.*, 2019, **151**, 74705.

104 H. Zhao, Z. Hu, L. Wei, P. Zeng, C. Kuang, X. Liu, S. Bai, F. Gao and M. Liu, *Small*, 2020, **16**, 2003939.

105 Y.-H. Kim, C. Wolf, Y.-T. Kim, H. Cho, W. Kwon, S. Do, A. Sadhanala, C. G. Park, S.-W. Rhee and S. H. Im, *ACS Nano*, 2017, **11**, 6586–6593.

106 R. E. Brandt, V. Stevanović, D. S. Ginley and T. Buonassisi, *MRS Commun.*, 2015, **5**, 265–275.

107 Y. Song, X. Zhang, L. Li, Z. Mo, J. Xu, S. Yu, X. Liu and J. Zhang, *Mater. Res. Express*, 2019, **6**, 115064.

108 S. Xu, A. Libanori, G. Luo and J. Chen, *Iscience*, 2021, **24**, 102235.

109 J. H. Noh, S. H. Im, J. H. Heo, T. N. Mandal and S. Il Seok, *Nano Lett.*, 2013, **13**, 1764–1769.

110 M. Branowski, P. Plochocka, R. Su, L. Legrand, T. Barisien, F. Bernardot, Q. Xiong, C. Testelin and M. Chamarro, *Photonics Res.*, 2020, **8**, A50–A55.

111 Q. Ma, S. Huang, X. Wen, M. A. Green and A. W. Y. Ho-Baillie, *Adv. Energy Mater.*, 2016, **6**, 1502202.

112 Q. Wang, J. A. Smith, D. Skroblin, J. A. Steele, C. M. Wolff, P. Caprioglio, M. Stolterfoht, H. Köbler, M. Li, S. H. Turren-Cruz, C. Gollwitzer, D. Neher and A. Abate, *Sol. RRL*, 2020, **4**, 1–9.

113 Y.-T. Yu, S.-H. Yang, L.-H. Chou, I. Osaka, X.-F. Wang and C.-L. Liu, *ACS Appl. Energy Mater.*, 2021, **4**, 5466–5474.

114 E. Breniaux, P. Dufour, S. Guillemet-Fritsch and C. Tenailleau, *Eur. J. Inorg. Chem.*, 2021, 3059–3073.

115 C. Zhang, Q. Wan, L. K. Ono, Y. Liu, W. Zheng, Q. Zhang, M. Liu, L. Kong, L. Li and Y. Qi, *ACS Energy Lett.*, 2021, **6**, 3545–3554.

116 A. Dutta, R. K. Behera, P. Pal, S. Baitalik and N. Pradhan, *Angew. Chem., Int. Ed.*, 2019, **58**, 5552–5556.

117 M. Imran, V. Caligiuri, M. Wang, L. Goldoni, M. Prato, R. Krahne, L. De Trizio and L. Manna, *J. Am. Chem. Soc.*, 2018, **140**, 2656–2664.

118 Y. Zhang, G. Li, C. She, S. Liu, F. Yue, C. Jing, Y. Cheng and J. Chu, *Nano Res.*, 2021, **14**, 2770–2775.

119 H. Huang, W. Zhao, H. Yang, X. Zhang, J. Su, K. Hu, Z. Nie, Y. Li and J. Zhong, *J. Mater. Chem. C*, 2021, **9**, 5535–5543.

120 L. Zhang, W. Liang, L. Xu, M. Zhu, X. Wang, J. Su, L. Li, N. Liu, Z. Zhang and Y. Gao, *Chem. Eng. J.*, 2021, **417**, 129349.

121 S. Zhou, C. Zhou, J. Zhu, H. Huang, F. Hu, Q. Ye, J. Zhong, X. Yang and H. Mao, *Appl. Surf. Sci.*, 2022, **578**, 152116.

122 D. Huang, J. Bo, R. Zheng, C. Luo, X. Sun, Q. Li, D. Shen, Z. Zheng, M. Chen and Y. Yang, *Adv. Opt. Mater.*, 2021, 2100474.

123 D. Zhou, R. Sun, W. Xu, N. Ding, D. Li, X. Chen, G. Pan, X. Bai and H. Song, *Nano Lett.*, 2019, **19**, 6904–6913.

124 N. Mondal, A. De and A. Samanta, *ACS Energy Lett.*, 2018, **4**, 32–39.

125 J. Wei, W. Zheng, P. Huang, Z. Gong, Z. Liu, S. Lu, Z. Li and X. Chen, *Nano Today*, 2021, **39**, 101179.

126 S. Ye, M. Yu, M. Zhao, J. Song and J. Qu, *J. Alloys Compd.*, 2018, **730**, 62–70.

127 S. Walck and T. Reinecke, *Phys. Rev. B: Condens. Matter Mater. Phys.*, 1998, **57**, 9088–9096.

128 P. Zhao, J. Su, Z. Lin, J. Wang, J. Zhang, Y. Hao, X. Ouyang and J. Chang, *Adv. Theory Simul.*, 2020, **3**, 1–9.

129 Y. Wang, F. Yang, X. Li, F. Ru, P. Liu, L. Wang, W. Ji, J. Xia and X. Meng, *Adv. Funct. Mater.*, 2019, **29**, 1–9.

130 Y. Gao, L. Zhao, Q. Shang, Y. Zhong, Z. Liu, J. Chen, Z. Zhang, J. Shi, W. Du and Y. Zhang, *Adv. Mater.*, 2018, **30**, 1801805.

131 D. Wang, J. Qiu, D. Zhou, S. Hu, Y. Wen, K. Zhang, Q. Wang, Y. Yang, H. Wu and Z. Long, *Chem. Eng. J.*, 2021, **421**, 127777.

132 W. Shi, Y. Zhao, C. Xie and P. Yang, *J. Lumin.*, 2021, **233**, 117886.

133 Y. Liu, G. Pan, R. Wang, H. Shao, H. Wang, W. Xu, H. Cui and H. Song, *Nanoscale*, 2018, **10**, 14067–14072.

134 H. Lin, Q. Wei, K. W. Ng, J. Dong, J. Li, W. Liu, S. Yan, S. Chen, G. Xing and X. Tang, *Small*, 2021, 2101359.

135 Z. Zhao, W. Xu, G. Pan, Y. Liu, M. Yang, S. Hua, X. Chen, H. Peng and H. Song, *Mater. Res. Bull.*, 2019, **112**, 142–146.

136 Q. Hu, J. Guo, M. Lu, P. Lu, Y. Zhang, W. W. Yu and X. Bai, *J. Phys. Chem. Lett.*, 2021, **12**, 8203–8211.

137 Z. He, X. Liang and W. Xiang, *Chem. Eng. J.*, 2022, **427**, 130964.

138 X. Zhou, Y. Zhao, W. Huang, Y. Wu, Z. Wu and G. He, *Org. Electron.*, 2021, 106253.

139 Y. Guo, J. Su, L. Wang, Z. Lin, Y. Hao and J. Chang, *J. Phys. Chem. Lett.*, 2021, **12**, 3393–3400.

140 K. Ma, Y. Sheng, G. Wang, X. Zhang, Y. Di, C. Liu, L. Yu, L. Dong and Z. Gan, *J. Lumin.*, 2021, 118622.

141 Z. Chen, H. He, Z. Wen, Z. Cui, S. Mei, D. Yang, X. Wei, W. Zhang, F. Xie and B. Yang, *Mater. Sci. Eng. B*, 2021, **273**, 115426.

142 H. Zhang, J. Yao, Y. Yang and H. Fu, *Chem. Mater.*, 2021, **33**, 2847–2854.

143 A. Forde, S. A. Thomas, R. J. Petersen, S. L. Brown, D. S. Kilin and E. K. Hobbie, *J. Phys. Chem. C*, 2021, **125**, 18849–18856.

144 Z.-J. Yong, S.-Q. Guo, J.-P. Ma, J.-Y. Zhang, Z.-Y. Li, Y.-M. Chen, B.-B. Zhang, Y. Zhou, J. Shu and J.-L. Gu, *J. Am. Chem. Soc.*, 2018, **140**, 9942–9951.

145 T. Chen, R. Liu, S. Tang, X. Li, S. Ye, X. Duan, R. Wang, Y. Shi, J. Yang and F. Qiu, *AIP Adv.*, 2021, **11**, 115008.

146 Y. Gao, C. Luo, C. Yan, W. Li, C. Liu and W. Yang, *J. Colloid Interface Sci.*, 2022, **607**, 1796–1804.

147 R. Wu, Z. Bai, J. Jiang, H. Yao and S. Qin, *RSC Adv.*, 2021, **11**, 8430–8436.

148 Y. Tong, Q. Wang, X. Liu, E. Mei, X. Liang and W. Xiang, *Chem. Eng. J.*, 2022, **429**, 132391.

3674 | *J. Mater. Chem. C*, 2022, **10**, 3647–3676

This journal is © The Royal Society of Chemistry 2022

149 Y. Li, Q. Liu, X. Liu, J. Feng, L. He, H. Li, C. Li and H. Zhang, *J. Phys. Chem. Lett.*, 2021, **12**, 10746–10752.

150 X. Li, Y. Wei, P. Dang, X. Xiao, H. Xiao, G. Zhang, G. Li and J. Lin, *Mater. Res. Bull.*, 2022, **146**, 111592.

151 D. Yan, Q. Mo, S. Zhao, W. Cai and Z. Zang, *Nanoscale.*, 2021, **13**, 9740–9746.

152 L. Xu, S. Yuan, H. Zeng and J. Song, *Mater. Today Nano*, 2019, **6**, 100036.

153 Y. Ji, J.-B. Zhang, H.-R. Shen, Z. Su, H. Cui, T. Lan, J.-Q. Wang, Y.-H. Chen, L. Liu and K. Cao, *ACS Omega*, 2021, **6**, 13831–13838.

154 J.-K. Chen, J.-P. Ma, S.-Q. Guo, Y.-M. Chen, Q. Zhao, B.-B. Zhang, Z.-Y. Li, Y. Zhou, J. Hou and Y. Kuroiwa, *Chem. Mater.*, 2019, **31**, 3974–3983.

155 Y. Zhao, C. Xie, X. Zhang, K. Matras-Postolek and P. Yang, *ACS Appl. Nano Mater.*, 2021, **4**, 6223–6230.

156 Z. Chen, L. Dong, C. Zhou, B. Zhou, Z. Zheng, R. Chen and J. Zang, *CrystEngComm*, 2021, **23**, 793–803.

157 Y. Gao, C. Yan, X. Peng, W. Li, J. Cao, Q. Wang, X. Zeng, X. Fu and W. Yang, *Nanoscale*, 2021, **13**, 18010–18031.

158 X. Shen, Y. Zhang, S. V. Kershaw, T. Li, C. Wang, X. Zhang, W. Wang, D. Li, Y. Wang and M. Lu, *Nano Lett.*, 2019, **19**, 1552–1559.

159 F. Qin, H. Tian, M. Yan, Y. Fang and D. Yang, *J. Mater. Chem. C*, 2021, **9**, 2016–2023.

160 J. Chen, Z. Shen, P. Liu, Z. Sun, J. G. Liu, C. Shen, D. Song, S. Zhao and Z. Xu, *Nanotechnology*, 2021, **32**, 325202.

161 S. Yang, H. Zhu, E. Xu, J. Li, H. Yang, Y. Zhang, Z. Zhu and Y. Jiang, *Nanotechnology*, 2021, **32**, 335601.

162 R. Chen, Y. Xu, S. Wang, C. Xia, Y. Liu, B. Yu, T. Xuan and H. Li, *J. Alloys Compd.*, 2021, **866**, 158969.

163 M. Rai, S. K. Singh, K. Mishra, R. Shankar, R. K. Srivastava and S. B. Rai, *J. Mater. Chem. C*, 2014, **2**, 7918–7926.

164 Q. Hu, Z. Li, Z. Tan, H. Song, C. Ge, G. Niu, J. Han and J. Tang, *Adv. Opt. Mater.*, 2018, **6**, 1–5.

165 G. Pan, X. Bai, D. Yang, X. Chen, P. Jing, S. Qu, L. Zhang, D. Zhou, J. Zhu, W. Xu, B. Dong and H. Song, *Nano Lett.*, 2017, **17**, 8005–8011.

166 L. Shao, D. Liu, J. Lyu, D. Zhou, N. Ding, R. Sun, W. Xu, N. Wang, S. Xu and B. Dong, *Mater. Today Phys.*, 2021, 100495.

167 M. Zeng, S. Singh, Z. Hens, J. Liu, F. Artizzu and R. Van Deun, *J. Mater. Chem. C*, 2019, **7**, 2014–2021.

168 X. Xu, Y. Sun, D. He, Z. Liang, G. Liu, S. Xu, Z. Li, L. Zhu and X. Pan, *J. Mater. Chem. C*, 2021, **9**, 208–213.

169 L. Zhou, T. Liu, J. Zheng, K. Yu, F. Yang, N. Wang, Y. Zuo, Z. Liu, C. Xue, C. Li, B. Cheng and Q. Wang, *J. Phys. Chem. C*, 2018, **122**, 26825–26834.

170 J. P. Ma, Y. M. Chen, L. M. Zhang, S. Q. Guo, J. D. Liu, H. Li, B. J. Ye, Z. Y. Li, Y. Zhou, B. Bin Zhang, O. M. Bakr, J. Y. Zhang and H. T. Sun, *J. Mater. Chem. C*, 2019, **7**, 3037–3048.

171 J. Duan, Y. Zhao, X. Yang, Y. Wang, B. He and Q. Tang, *Adv. Energy Mater.*, 2018, **8**, 1–9.

172 L. Chen, W. Wu, J. Wang, Z. Qian, R. Liu, Y. Niu, Y. Chen, X. Xie and H. Zhang, *ACS Appl. Energy Mater.*, 2021, **4**, 3937–3944.

173 H. Huang, R. Li, S. Jin, Z. Li, P. Huang, J. Hong, S. Du, W. Zheng, X. Chen and D. Chen, *ACS Appl. Mater. Interfaces*, 2021, **13**, 34561–34571.

174 X. Zhang, Y. Zhang, X. Zhang, W. Yin, Y. Wang, H. Wang, M. Lu, Z. Li, Z. Gu and W. W. Yu, *J. Mater. Chem. C*, 2018, **6**, 10101–10105.

175 M. Rai, S. K. Singh, A. K. Singh, R. Prasad, B. Koch, K. Mishra and S. B. Rai, *ACS Appl. Mater. Interfaces*, 2015, **7**, 15339–15350.

176 A. K. Singh, *Coord. Chem. Rev.*, 2022, **455**, 214365.

177 Q. Cao, A. Ilyas, S. Zhang, Z. Ju, F. Sun, T. Liu, Y. M. Yang, Y. H. Lu and X. Liu, *Nanoscale*, 2021, **13**, 11552–11560.

178 L. Wang, H. Zhou, J. Hu, B. Huang, M. Sun, B. Dong, G. Zheng, Y. Huang, Y. Chen and L. Li, *Science*, 2019, **363**, 265–270.

179 A. K. Jena, A. Kulkarni, Y. Sanehira, M. Ikegami and T. Miyasaka, *Chem. Mater.*, 2018, **30**, 6668–6674.

180 J. Shi, F. Li, J. Yuan, X. Ling, S. Zhou, Y. Qian and W. Ma, *J. Mater. Chem. A*, 2019, **7**, 20936–20944.

181 B. Wang, L. Liu, B. Liu, J. Li, B. Cao, Z. Zhao and Z. Liu, *Phys. B*, 2020, **599**, 412488.

182 G. Pan, X. Bai, W. Xu, X. Chen, D. Zhou, J. Zhu, H. Shao, Y. Zhai, B. Dong, L. Xu and H. Song, *ACS Appl. Mater. Interfaces*, 2018, **10**, 39040–39048.

183 J.-P. Ma, Y.-M. Chen, L.-M. Zhang, S.-Q. Guo, J.-D. Liu, H. Li, B.-J. Ye, Z.-Y. Li, Y. Zhou and B.-B. Zhang, *J. Mater. Chem. C*, 2019, **7**, 3037–3048.

184 Y. Zhu, B. Yang, Q. Lu, L. Zhang, Y. Zhao, B. Xia, S. Mei, M. Shi, Y. Li and R. Hu, *J. Non Cryst. Solids*, 2022, **575**, 121224.

185 L. Yuan, L. Zhou, W. Xiang and X. Liang, *J. Non Cryst. Solids*, 2020, **545**, 120232.

186 S. K. Karunakaran, G. M. Arumugam, W. Yang, S. Ge, S. N. Khan, Y. Mai, X. Lin and G. Yang, *Sol. RRL*, 2020, 2000390.

187 W. Xiang, Z. Wang, D. J. Kubicki, W. Tress, J. Luo, D. Prochowicz, S. Akin, L. Emsley, J. Zhou, G. Dietler, M. Grätzel and A. Hagfeldt, *Joule*, 2019, **3**, 205–214.

188 M. Wang, K. Deng, L. Meng and L. Li, *Small Methods*, 2020, **4**, 1–8.

189 Y. Xie, B. Peng, I. Bravić, Y. Yu, Y. Dong, R. Liang, Q. Ou, B. Monserrat and S. Zhang, *Adv. Sci.*, 2020, **7**, 28–30.

190 C. Zhang, A. Zhang, T. Liu, L. Zhou, J. Zheng, Y. Zuo, Y. He and J. Li, *RSC Adv.*, 2020, **10**, 17635–17641.

191 W. J. Mir, T. Sheikh, H. Arfin, Z. Xia and A. Nag, *NPG Asia Mater.*, 2020, **12**, 1–9.

192 T. J. Milstein, D. M. Kroupa and D. R. Gamelin, *Nano Lett.*, 2018, **18**, 3792–3799.

193 M. Zeng, F. Locardi, D. Mara, Z. Hens, R. Van Deun and F. Artizzu, *Nanoscale*, 2021, **13**, 8118–8125.

194 X. Li, Y. Yu, J. Hong, Z. Feng, X. Guan, D. Chen and Z. Zheng, *J. Lumin.*, 2020, **219**, 116897.

This journal is © The Royal Society of Chemistry 2022

J. Mater. Chem. C, 2022, **10**, 3647–3676 | **3675**

195 Y. Zhang, J. Liu, H. Zhang, Q. He, X. Liang and W. Xiang, *J. Eur. Ceram. Soc.*, 2020, **40**, 6023–6030.

196 G. Yao, S. Li, D. Valiev, Q. Chen, Y. Hu, L. Jia, S. Stepanov, Y. Zhou, C. Li and Z. Su, *Opt. Mater.*, 2021, **122**, 111711.

197 Y. Yu, G. Shao, L. Ding, H. Zhang, X. Liang, J. Liu and W. Xiang, *J. Rare Earths*, 2021, **39**, 1497–1505.

198 P. Feng, X. Yang, X. Feng, G. Zhao, X. Li, J. Cao, Y. Tang and C.-H. Yan, *ACS Nano*, 2021, **15**, 6266–6275.